

Mapping the core of the Tarantula Nebula with VLT-MUSE. III. A template for metal-poor starburst regions in the visual and far-ultraviolet

Paul A. Crowther¹*, N. Castro²

¹ Department of Physics and Astronomy, University of Sheffield, Sheffield, S3 7RH, UK

² Leibniz-Institut für Astrophysik Potsdam, An der Sternwarte 16, 14482 Potsdam, Germany

Accepted 2023 November 24. Received 2023 November 24; in original form 2023 September 19

ABSTRACT

We present the integrated VLT-MUSE spectrum of the central $2' \times 2'$ ($30 \times 30 \text{ pc}^2$) of NGC 2070, the dominant giant H II region of the Tarantula Nebula in the Large Magellanic Cloud, together with an empirical far-ultraviolet spectrum constructed via LMC template stars from the ULLYSES survey and Hubble Tarantula Treasury Project UV photometry. NGC 2070 provides a unique opportunity to compare results from individual stellar populations (e.g. VLT FLAMES Tarantula Survey) in a metal-poor starburst region to the integrated results from the population synthesis tools Starburst99, Charlot & Bruzual and BPASS. The metallicity of NGC 2070 inferred from standard nebular strong line calibrations is $\sim 0.4 \pm 0.1$ dex lower than obtained from direct methods. The H α inferred age of 4.2 Myr from Starburst99 is close to the median age of OB stars within the region, although individual stars span a broad range of 1–7 Myr. The inferred stellar mass is close to that obtained for the rich star cluster R136 within NGC 2070, although this contributes only 21% to the integrated far-UV continuum. He II $\lambda 1640$ emission is dominated by classical WR stars and main sequence WNh+Of/WN stars. 18% of the NGC 2070 far UV continuum flux arises from very massive stars with $\geq 100 M_\odot$, including several very luminous Of supergiants. None of the predicted population synthesis models at low metallicities are able to successfully reproduce the far-UV spectrum of NGC 2070. We attribute issues to the treatment of mass-loss in very massive stars, the lack of contemporary empirical metal-poor templates, plus WR stars produced via binary evolution.

Key words: stars: massive - galaxies: Magellanic Clouds; galaxies: starburst; galaxies: clusters: individual: R136; ISM: HII regions: ultraviolet: stars

1 INTRODUCTION

The Tarantula Nebula (30 Doradus) in the Large Magellanic Cloud (LMC) is intrinsically the brightest star-forming region within the Local Group of galaxies (Crowther 2019). It has been the subject of numerous studies across the electromagnetic spectrum (Vacca et al. 1995; Sabbi et al. 2013; Wong et al. 2022; Crowther et al. 2022; Fahrion & De Marchi 2023). Its low (half-solar) metallicity and high star-formation intensity are more typical of knots star-forming galaxies at $z \sim 2$ –3 (Steidel et al. 2016; Johnson et al. 2017) than local systems, owing to its very rich stellar content (Schneider et al. 2018a). Indeed, 30 Doradus has nebular conditions which are reminiscent of Green Pea galaxies (Cardamone et al. 2009), which are local extreme emission-line galaxies, some of which are known to be Lyman continuum leakers (Micheva et al. 2017).

The Tarantula Nebula is host to hundreds of massive stars, including very massive stars (VMS) located in the central, dense star cluster R136 (Massey & Hunter 1998; Crowther et al. 2010) and the extended giant H II region NGC 2070, the central ionized nebula within the Tarantula (Bestenlehner et al. 2014). Its proximity permits observation and analysis of individual massive OB and Wolf-Rayet stars (Melnick 1985; Selman et al. 1999; Evans et al. 2011). Star

formation in the Tarantula Nebula began at least 15–30 Myr ago, as witnessed by the Hodge 301 cluster, with an upturn in its rate of star formation in the last 5–10 Myr (Schneider et al. 2018b). Star formation is still ongoing, as witnessed by clumps of molecular gas observed with the Atacama Large Millimeter Array (ALMA, Wong et al. 2022).

The proximity of the LMC provides a unique opportunity to study a rich, intensively star-forming region individually, via its resolved stellar content (Doran et al. 2013), and collectively, via its integrated light via application of population synthesis models. If the LMC were located at a distance of 10 Mpc, R136, NGC 2070 and the Tarantula would subtend diameters of 0.04 arcsec, 0.8 arcsec and 6 arcsec, respectively (Crowther 2019). Population synthesis models are widely employed to interpret far-UV spectroscopy of unresolved star clusters at Mpc distances (Chandar et al. 2004; James et al. 2014; Sirressi et al. 2022), local star-forming galaxies (Wofford et al. 2013; Berg et al. 2022) plus those at $z > 2$ observed with large ground-based telescopes (Steidel et al. 2016; Saxena et al. 2020) or *James Webb Space Telescope* (Carnall et al. 2023; Curtis-Lake et al. 2023).

Although the nebular properties of the entire 30 Doradus region has previously been studied (Kennicutt et al. 1995; Pellegrini et al. 2010), here we focus on the central region of NGC 2070 observed with the Multi Unit Spectroscopic Explorer (MUSE) mounted at the Very Large Telescope (VLT), as part of its original Science

* paul.crowther@sheffield.ac.uk

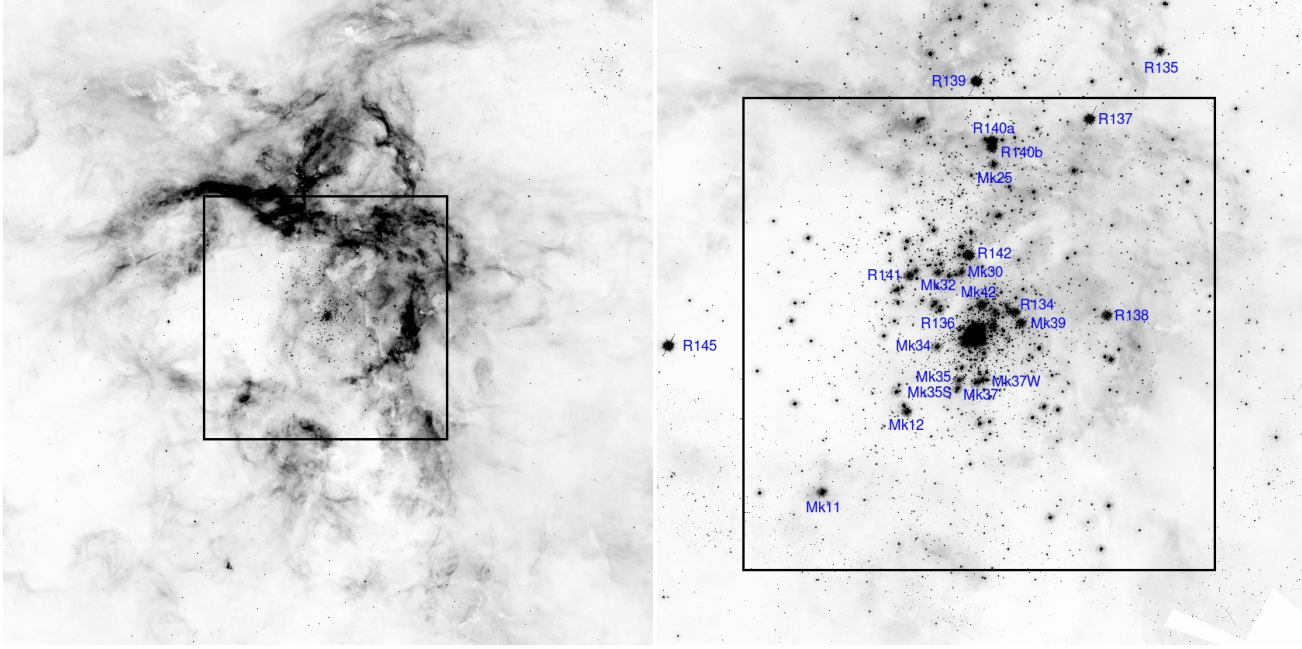


Figure 1. Left panel: HST ACS/F658N image of the central region of 30 Doradus (320×320 arcsec 2) from HTTP (Sabbi et al. 2013) including MUSE field of view (black box). North is up, East to the left. Hodge 301 can be seen to the upper right. Right panel: HST WFC3/F336W image of central region of NGC 2070 (165×165 arcsec 2) from HTTP, with selected bright sources labelled. The white region to the lower right is not included in the F336W footprint

Verification programme. Castro et al. (2018) introduce the dataset, and provide a stellar census and nebular kinematic properties, while Castro et al. (2021b) present a spectroscopic analysis of OB stars. This region is host to the central R136 star cluster, several WR stars including the R140 complex, plus several cool supergiants such as Melnick 9.

Age estimates of OB stars within NGC 2070 (external to R136) range from 1–7 Myr, with a median age of 3.6 Myr (Schneider et al. 2018b). To date, only the central cluster R136 has been observed in the far-ultraviolet, both collectively (Heap et al. 1992) and individually (Crowther et al. 2016), the latter obtaining a cluster age of ~ 1.5 Myr (see also Brands et al. 2022). Several other luminous early-type stars within NGC 2070 have been observed in the far-UV with COS or STIS instruments aboard *Hubble Space Telescope* (HST), plus a large sample of far-UV template spectra of LMC OB stars have been obtained via the *HST* initiative ULLYSES (Roman-Duval et al. 2020; Crowther 2022). Consequently we are able to construct an empirical integrated spectrum of the MUSE field-of-view in the far-UV, for comparison with predictions from (theoretical) population synthesis models Starburst99 (Leitherer et al. 1999, 2014), Charlot & Bruzual (Bruzual & Charlot 2003; Plat et al. 2019), and BPASS (Eldridge et al. 2017; Stanway & Eldridge 2018).

The present study completes the analysis of NGC 2070 MUSE Wide Field Mode (WFM) observations and is structured as follows. We provide a brief summary of visual MUSE observations of NGC 2070 and describe how the far-UV spectrum of NGC 2070 is constructed in Section 2. The integrated MUSE dataset is analysed in Section 3, with an emphasis on nebular properties and optical Wolf-Rayet bumps, with the far-UV spectrum compared to predictions from various population synthesis models in Section 4. A comparison between individual and cumulative results is provided in Section 5, together with brief conclusions. Initial results for nebular, stellar and integrated properties of the MUSE WFM datasets were presented in Crowther et al. (2017).

2 NGC 2070 SPECTROSCOPIC DATASETS

2.1 Visual observations

MUSE is a wide-field, integral-field spectrograph providing intermediate resolution ($R \sim 2000$) spectroscopy from 4600–9350Å (Bacon et al. 2010). Four overlapping MUSE Wide Field Mode pointings were obtained at the Very Large Telescope (VLT) in August 2014 via a Science Verification programme (PI: J. Melnick), providing a 2×2 arcmin 2 (30×30 pc 2) mosaic which encompasses both the R136 star cluster and R140, an aggregate of WR stars to the north (Castro et al. 2018). The MUSE field of view is indicated on Hubble Tarantula Treasury Project¹ (HTTP, Sabbi et al. 2013). 320×320 arcsec 2 ACS/F658N and 165×165 arcsec 2 WFC3/F336W images in Fig. 1 in which selected bright sources are identified in the latter. A larger footprint, especially to the north, would be required to fully sample the bright nebulosity of NGC 2070, but MUSE field of view includes $\sim 50\%$ of the far-UV continuum of the entire Tarantula².

The MUSE spatial resolution spanned 0.7 to 1.1 arcsec, corresponding to a mean spatial resolution of 0.22 ± 0.04 pc. Four exposures of 600s for each pointing provided a continuum S/N exceeding 50 for 600 sources in the yellow. The integrated MUSE green-red spectrum of NGC 2070 is presented in Fig. 2, with nebular properties reminiscent of Green Pea galaxies (Cardamone et al. 2009), plus WR bumps in the blue (upper inset) and red (lower inset). Recent MUSE Narrow Field Mode (NFM) observations of the R136 cluster are presented in Castro et al. (2021a).

¹ <https://archive.stsci.edu/hlsp/http>

² We have followed the approach set out in Section 2.2 to estimate $F_{1500} \sim 1.2 \times 10^{-11}$ erg s $^{-1}$ cm $^{-2}$ Å $^{-1}$ for the region of the Tarantula exterior to the MUSE footprint

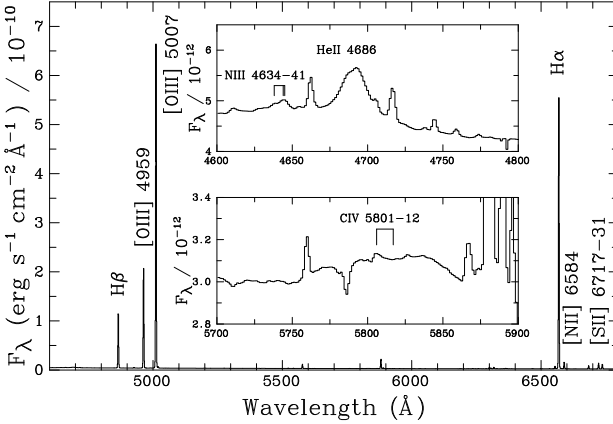


Figure 2. Integrated MUSE spectrum of NGC 2070, updated from Crowther et al. (2017), revealing a striking emission line spectrum, with nebular properties (e.g. high [O III] $\lambda\lambda$ 5007/H β , low [N II] $\lambda\lambda$ 6584/H α) reminiscent of Green Pea galaxies (Cardamone et al. 2009). WR bumps are observed in the blue (upper inset, He II $\lambda\lambda$ 4686 arising from primarily WN stars) and yellow (lower inset, C IV $\lambda\lambda$ 5801-12 due to WC stars). Nebular lines in the insets include [Fe III] λ 4658, [Ar IV] λ 4711, [N II] λ 5755 and He I λ 5876.

Table 1. Summary of sources brighter than $F_{1500} = 10^{-14}$ erg s $^{-1}$ cm $^{-2}$ Å $^{-1}$ contributing to the far-UV continuum of the MUSE pointing, broken down by subtype (primary in binaries) and whether empirical UV spectroscopy or templates were utilised. The R136a GHRS spectrum comprises 3 WNH stars and 26 O stars (assuming HSH95-17 is an O star, Kalari et al. (2022)), each contributing ~40% and 60% of the far-UV flux of R136a. 20 sources are confirmed spectroscopic binaries, comprising 15 systems with an O-type primary, 3 with an Of/WN or WN5h primary, plus 1 each with a Wolf-Rayet or B-type primary. 180 additional faint sources with $5 \times 10^{-16} \leq F_{1500} < 1.0 \times 10^{-14}$ erg s $^{-1}$ cm $^{-2}$ Å $^{-1}$ are incorporated via a B0 V template scaled to the sum of their far-UV fluxes.

Subtype	Empirical		Template		Total	
	N	F_{1500}	N	F_{1500}	N	F_{1500}
O	34	1.92×10^{-12}	159	7.44×10^{-12}	193	9.36×10^{-12}
Of/WN+WNh	7	1.31×10^{-12}	5	0.46×10^{-12}	12	1.77×10^{-12}
B	0	...	16	1.40×10^{-12}	16	1.40×10^{-12}
Wolf-Rayet	1	0.39×10^{-12}	5	0.67×10^{-12}	6	1.06×10^{-12}
Sum	42	3.62×10^{-12}	185	9.97×10^{-12}	227	13.59×10^{-12}
Sum + Faint	180	0.83×10^{-12}	407	14.42×10^{-12}

2.2 Far-ultraviolet observations

The combination of VLT/MUSE (Castro et al. 2018), VLT/FLAMES (Evans et al. 2011) and HST/STIS (Crowther et al. 2016) spectroscopy provide near complete spectral type census of bright early-type stars in the Tarantula (Schneider et al. 2018a; Crowther 2019). This census permits us to construct an integrated far-UV spectrum of the region within the MUSE mosaic discussed in Section 2.1, by combining empirical datasets for a subset of stars (those with far-UV spectroscopy) with suitable templates for the remainder (those lacking far-UV spectroscopy at $R \geq 2000$). Empirical HST COS or STIS spectroscopy is available for a subset of individual UV-bright sources, which are rebinned to $R \sim 2000$. These are supplemented by Goddard High Resolution Spectroscopy (GHRS) G140L observations of the central 2×2 arcsec 2 R136a cluster (Heap et al. 1992), also obtained at

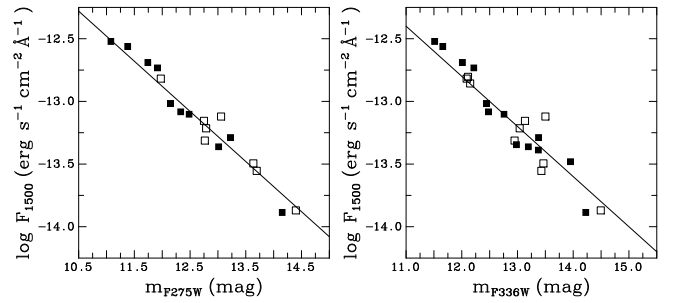


Figure 3. Relationship between m_{F275W} (left) or m_{F336W} (right) and far-UV flux, F_{1500} , for O stars in 30 Doradus (solid within MUSE field) with far-UV spectroscopy and HST/WFC3 photometry (Sabbi et al. 2013). The solid line is a linear fit to all observations.

$R \sim 2000$ ³. The cumulative far-UV spectrum was constructed using the Starlink spectroscopic package DIPSO (Howarth et al. 2004).

For the majority of sources, far-UV spectroscopy of LMC OB and WR templates from ULLYSES⁴ (Roman-Duval et al. 2020) are utilised (up to DR6), supplemented by COS and STIS datasets from GO programmes (GO 15629, Mahy; GO 16272, Shenar). Templates are anchored to estimates of 1500Å fluxes determined from F275W or F336W photometry from HTTP (Sabbi et al. 2016). Since HTTP photometry of 30 Doradus is incomplete, we also utilise WFC3/F336W photometry from De Marchi et al. (2011) or WFPC2/F336W photometry from Hunter et al. (1995). We provide details of templates in Tables A1-A2. Gaps in spectra arise from incomplete spectral coverage (e.g. COS G130M+G160M).

We estimate $\lambda 1500$ fluxes of O and WR stars lacking far-UV spectroscopy from a calibration of F275W photometry anchored by O stars within 30 Doradus for which far-UV spectroscopy is available, as shown in the left panel of Fig 3, whose linear fit is

$$\log F_{1500} = -0.4(m_{F275W} + 20.20 \pm 0.08) \quad (1)$$

F275W photometry is not available throughout the MUSE field of view, whereas F336W is available for all sources, for which a calibration is presented in the right panel of Fig. 3, and a linear fit is

$$\log F_{1500} = -0.4(m_{F336W} + 20.00 \pm 0.15). \quad (2)$$

Fluxes for individual stars in 30 Doradus used in the calibration are provided in Appendix C (Table C1). For B supergiants, $\lambda 1500$ fluxes are reduced by a scale factor of 0.85 (B0.5±0.5), 0.65 (B1–3) or 0.5 (B4–9) from a comparison between spherical non-LTE model atmospheres of far- to near-UV fluxes of O and B stars (Hillier & Miller 1998). For B dwarfs, $\lambda 1500$ fluxes are reduced by a factor of 0.77 (B0.5±0.5) or 0.65 (B1.5±0.5) from a comparison between TLUSTY plane parallel non-LTE model atmospheres of O and B stars (Lanz & Hubeny 2007). We also adjust the $\lambda\lambda 1160$ –1700 slopes of templates according to their $m_{F336W} - m_{F555W}$ colours as discussed in Appendix C

We incorporate a total of 227 sources with spectral types and estimated fluxes $F_{1500} \geq 10^{-14}$ erg s $^{-1}$ cm $^{-2}$ Å $^{-1}$ into our cumulative far-UV spectrum, which are listed in Appendix B (Table B1). Of

³ The spectral resolution of STIS/G140L observations from Crowther et al. (2016) achieved $R \sim 1000$, too low for our purposes here

⁴ <https://ullyses.stsci.edu/>

these, 29 lie within the R136a 2×2 arcsec 2 GHRS footprint, 13 possess HST COS (G130M+G160M or G140L) or STIS (E140M) spectroscopy, such that the remaining 185 require ULLYSES templates, several of which have known far-UV fluxes courtesy of HST/STIS G140L spectroscopy (Massey et al. 2005). Although R136a stars exterior to the GHRS footprint have been observed in the far-UV with HST/STIS G140L (Crowther et al. 2016), their slit loss corrections are uncertain, such that F_{1500} from GHRS is $\sim 20\%$ higher than the sum of individual fluxes. Consequently we adopt F_{1500} from calibrations for stars exterior to the GHRS aperture in common with (Crowther et al. 2016).

HSH95 17, alias #9 from Kalari et al. (2022), is included in Table B1 despite an uncertain spectral type since it lies within the GHRS 2×2 arcsec 2 footprint such that we do not require a bespoke UV template. Several other sources which would qualify on the basis of their far-UV fluxes are excluded due to unknown spectral types (e.g. HSH95 76, HSH95 87, SMB 136) which is necessary to incorporate suitable UV templates. Their contribution to the cumulative far-UV flux is negligible ($\sim 1\%$).

20 sources in Table B1 are confirmed spectroscopic binaries, although not all stars have been subject to spectroscopic monitoring, so the true binary frequency will be significantly higher. Confirmed multiple systems amongst the UV-brightest sources ($F_{1500} \geq 5 \times 10^{-14}$ erg s $^{-1}$ cm $^{-2}$ Å $^{-1}$) include O-type binaries HSH95 39, HSH95 42 within R136a (Massey et al. 2002), Wolf-Rayet and O-type binaries R140b, c and d (Shenar et al. 2019; Walborn et al. 2014), plus colliding wind binaries R136c, Mk 33Na, Mk 34 and Mk 39 (Crowther et al. 2022).

The cumulative far-UV flux of the individual 227 sources is 1.36×10^{-11} erg s $^{-1}$ cm $^{-2}$ Å $^{-1}$. An additional 180 sources with known spectral types possess far-UV fluxes in the range $5 \times 10^{-16} \leq F_{1500} < 1.0 \times 10^{-14}$ erg s $^{-1}$ cm $^{-2}$ Å $^{-1}$. We account for these collectively via a B0 V template scaled to their cumulative far-UV flux (8.35×10^{-13} erg s $^{-1}$ cm $^{-2}$ Å $^{-1}$), such that they contributes an additional $\sim 6\%$ to the total far-UV continuum. Table 1 provides a spectral subtype of the sources contributing to the far-UV continuum. Stars possessing empirical far-UV spectroscopy contribute 25% of the total. The dominant contribution arises from large numbers of O stars (65%), although modest populations of very massive main-sequence WN (WNh) and transition Of/WN stars (12%), B stars, primarily supergiants (10%) and classical WR stars (7%) also make non-negligible contributions.

Fig. 4 presents the cumulative far-UV spectrum of the MUSE field, including contributions from OB-type (pink), classical WR (blue) stars plus main sequence WNh and Of/WN stars (red). We have split relative contributions from O and WNh stars to the core of R136a by adjusting their combined HST STIS/G140L spectra from (Crowther et al. 2016) to the flux of the HST/GHRS spectrum. He II $\lambda 1640$ is unusually strong ($W_\lambda = 4.7 \pm 0.2$ Å) and broad (FWHM = 9.3 ± 0.3 Å). Figs A1–A4 in Appendix A illustrate the contribution of empirical datasets and templates to the far-UV spectra of individual spectral types. All subtypes contribute to the strong CIV $\lambda 1550$ P Cygni profile, although it is apparent that He II $\lambda 1640$ emission is dominated by classical WR stars (56%) plus WNh and Of/WN stars (31%). All subtypes contribute to N V $\lambda 1240$, aside from B supergiants, although B supergiants and classical WR stars are the primary contributors to P Cygni Si IV $\lambda 1400$.

In Table B1 we have flagged ~ 18 Very Massive Stars (VMS) with initial masses in excess of $\sim 100 M_\odot$ on the basis of spectroscopic results (Bestenlehner et al. 2014; Tehrani et al. 2019; Brands et al. 2022). The majority of these have WNH5, Of/WN or O2–4 If spectral types, exceptions include R136a7 (O3 III(f*)), R136a4 (O3 V) and

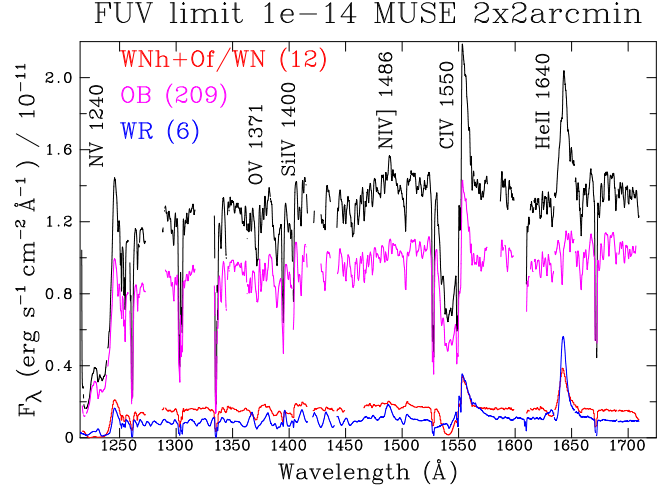


Figure 4. Cumulative far-UV spectrum of the central region of NGC 2070 (black) inferred from a combination of empirical (42 stars, 25% of total), LMC templates (185 stars, 69% of total) plus faint OB stars (180 stars, 6% of total), highlighting contributions from OB stars (pink), Of/WN and WNH stars (red), and classical WR stars (blue). He II $\lambda 1640$ emission is dominated by classical WR stars (56%) and very massive main sequence stars (31%), with the remainder arising from Of supergiants (e.g. Mk 42, R136a5). Gaps in spectra arise from incomplete spectral coverage of templates (e.g. COS G130M+G160M).

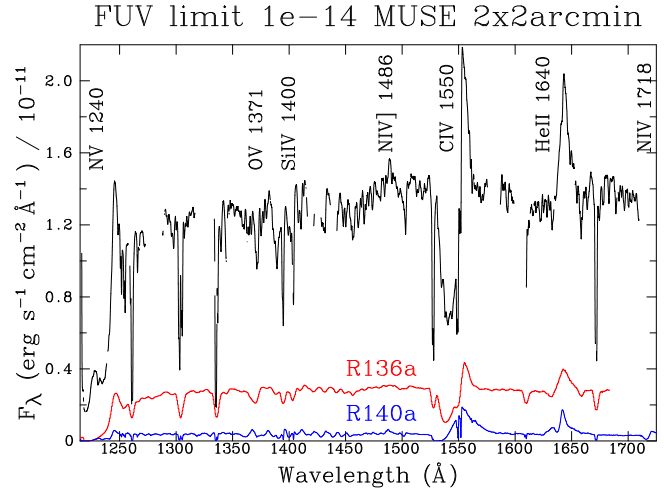


Figure 5. Cumulative far-UV spectrum of the central region of NGC 2070 (black) together with the integrated STIS/G140L spectrum of the R136a cluster (red, 3.6×3.6 arcsec 2) from Crowther et al. (2016) plus STIS/E140M spectrum of R140a (blue), the UV brightest source in the MUSE field, which is host to classical WN+WC stars. Gaps in spectra arise from incomplete spectral coverage of templates (e.g. COS G130M+G160M).

VFTS 506 (ON2 V). In spite of their scarcity, 18% of the NGC 2070 far UV flux arises from VMS.

Fig. 5 compares the cumulative far-UV spectrum to the integrated STIS/G140L spectrum of R136a from Crowther et al. (2016), contributing 22% of the far-UV continuum flux, plus the STIS/E140M spectrum of R140a (VFTS 507), the brightest individual source in the MUSE field (3% of far-UV continuum flux), host to classical WN+WC stars. Neither of the WR stars within R140a are known to be binaries (Bartzakos et al. 2001; Shenar et al. 2019), although the complete stellar content of R140a remains uncertain. R136a pos-

Table 2. Primary contributors to the integrated He II $\lambda 1640$ emission line (F_{1640} units of $10^{-12} \text{ erg s}^{-1} \text{ cm}^{-2}$) in the central $30 \times 30 \text{ pc}^2$ region of NGC 2070, including the cumulative line flux from the central cluster R136a which is dominated by WN5h stars R136a1, a2 and a3 (Crowther et al. 2016). Details of templates are provided in Table A2.

Source	Sp Type	F_{1640}	Obs	VMS
R136a	3xWN5h+O4 If/WN8+..	13.	STIS/G140L	8✓
R140a	WC4+WN6+..	12.	STIS/E140M	...
R140b	WN5(h)+O	9.	WN6 template	...
R134	WN6(h)	6.5	WN6 template	...
Mk 53	WN8(h)	2.2	WN7 template	...
Mk 49	WN6(h)	2.1	WN6 template	...
Mk 33Sb	WC5	2.1	WC4 template	...
R136c	WN5h+	1.8	WN5h template	✓
Mk 34	WN5h+WN5h	1.6	WN5h template	2✓
Mk 39	O2.5 If/WN6+	1.1	COS/G130M+G160M	✓
Mk 42	O2 If*	0.8	STIS/E140M	✓
Mk 35	O2 If/WN5	0.8	O2If/WN5 template	✓
Mk 37a	O3.5 If/WN7	0.5	O3.5 If/WN7 template	✓
Total		57.

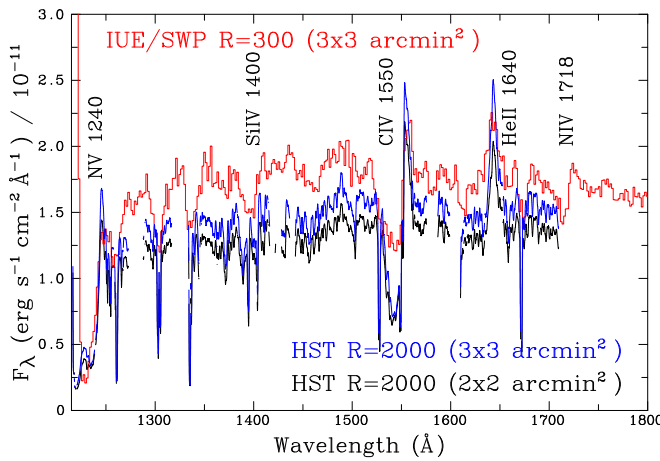


Figure 6. Integrated IUE/SWP spectra of the central $3' \times 3'$ (red) region of NGC 2070 from Vacca et al. (1995) together with our cumulative far-UV spectrum for the central $2' \times 2'$ (black) and $3' \times 3'$ (blue) regions. N IV $\lambda 1718$ is prominent in the large aperture IUE dataset despite its low ($R \sim 300$) spectral resolution. IUE observations suggest 15% higher far-UV flux levels owing to a combination of flux calibration differences or unresolved stars (primarily B-type) omitted from our study.

sesses an extremely strong He II $\lambda 1640$ emission with respect to typical young star clusters, but the richness of the surrounding massive star population in NGC 2070 is such that it only contributes a quarter of the integrated emission line flux of He II $\lambda 1640$. Table 2 lists the primary contributors to F_{1640} , the majority of which originates from classical WR stars, notably R140a.

Vacca et al. (1995) have previously scanned NGC 2070 with IUE with the short wavelength camera (SWP), at low spectral resolution ($R \sim 300$) using the large $10'' \times 20''$ aperture, providing integrated spectra for the central $20'' \times 20''$, $1' \times 1'$, and $3' \times 3'$ regions. Fig. 6 compares the integrated spectrum of the central $3' \times 3'$ region (red) with our cumulative far-UV spectrum of the $2' \times 2'$ MUSE region (black). The overall shape of the spectra are similar, but the

continuum flux of our far-UV spectrum is only $\sim 80\%$ of the large IUE aperture. N IV $\lambda 1718$ is prominent in the large aperture IUE dataset despite its low spectral resolution.

Table B2 lists additional stars with known spectral types brighter than $1.0 \times 10^{-14} \text{ erg s}^{-1} \text{ cm}^{-2} \text{ Angstrom}^{-1}$ within the large $3' \times 3'$ IUE aperture. These increase the far-UV continuum flux by $1.7 \times 10^{-12} \text{ erg s}^{-1} \text{ cm}^{-2} \text{ Angstrom}^{-1}$, the majority of which is supplied by R135, R139 and R145. Owing to their relative isolation (Fig. 1), far-UV flux levels for these three bright stars are drawn from low-resolution IUE/SWP large aperture spectroscopy (Fitzpatrick & Savage 1984).

The blue spectrum in Fig. 6 additionally incorporates all stars listed in Table B2, and reveals a difference of $\sim 15\%$ in global far-UV flux levels between IUE and our approach using HST observations. The difference likely arises from the combination of absolute flux calibration and the omission of a diffuse far-UV background from unresolved stars in our study – recall 20% of the integrated far-UV continuum of the rich R136 cluster was from an intra-cluster background (Crowther et al. 2016). Collectively, B-type main sequence stars – lacking strong UV wind features – will dominate this population.

3 ANALYSIS OF INTEGRATED VISUAL SPECTROSCOPY

3.1 Nebular properties

As shown in Fig. 2, the integrated MUSE spectrum of NGC 2070 is dominated by nebular emission lines, plus broad, weak Wolf-Rayet features. Here we undertake an analysis of the nebular spectrum with a focus on the inferred metallicity and age/mass of the ionizing stellar population using commonly used spectral synthesis tools Starburst99 (version 7.0.1, Leitherer et al. 1999, 2014), Charlot & Bruzual (Bruzual & Charlot 2003; Plat et al. 2019, CB19,I) and BPASS (v.2.2.1, Eldridge et al. 2017; Stanway & Eldridge 2018). A detailed study of the integrated 30 Doradus nebula has been undertaken by Pellegrini et al. (2011) while Peimbert (2003) utilise VLT/UVES spectroscopy for a detailed chemical analysis.

Table 3 presents measured MUSE line fluxes, intensities and luminosities (assuming 50 kpc), the former obtained using the elf suite within the Starlink package DIPSO (Howarth et al. 2004). Although 30 Doradus is known to have a non-standard dust extinction (Maíz Apellániz et al. 2014; De Marchi & Panagia 2014; Brands et al. 2023), we shall adopt a standard LMC extinction law with $R_V = 3.1$ (Howarth 1983) for the nebular analysis. We obtain $c(H\beta) = 0.54$ from $I(H\alpha)/I(H\beta) = 2.86$ for Case B recombination theory for a standard $N_e = 10^2 \text{ cm}^{-3}$ and $T_e = 10^4 \text{ K}$ – these results are consistent with averages of resolved maps from Castro et al. (2018).

$L(H\alpha) = 1.37 \times 10^{39} \text{ erg s}^{-1}$ equates to an ionizing output of $10^{51} \text{ ph s}^{-1}$, corresponding to a star formation rate of $0.005 M_\odot \text{ yr}^{-1}$ using standard conversions from Kennicutt (1998). Our MUSE dataset of the central region of NGC 2070 ($30 \times 30 \text{ pc}^2$) lies within the extended 30 Doradus region. Pellegrini et al. (2010) have investigated a much larger $140 \times 80 \text{ pc}^2$ region, and highlighted that 50% of the integrated H α emission originates from relatively low surface brightness regions.

We used the temden routine in IRAF to determine the nebular density and temperature. We obtain $N_e = 240 \pm 10 \text{ cm}^{-3}$ from the standard [S II] 6717/6731 diagnostic, and $N_e = 310^{+220}_{-250} \text{ cm}^{-3}$ from the weak [Cl III] 5518/5538 diagnostic. Comparable results are obtained from the [Fe III] 4658/4986 ratio (Keenan et al. 2001). The usual [O III] 4363/5007 temperature diagnostic is not available for MUSE observations at $z = 0$, so we use [N II] 5755/6584 to obtain

Table 3. Fluxes (F), intensities (I) and luminosities (L) of nebular emission lines and Wolf-Rayet (WR) bumps in the integrated MUSE spectrum of the 2×2 arcmin central region of NGC 2070. Case B recombination theory is adopted together with a standard LMC extinction law (Howarth 1983) and an adopted LMC distance of 50 kpc.

Line	F $10^{-11} \text{ erg s}^{-1} \text{ cm}^{-2}$	I $10^{-10} \text{ erg s}^{-1} \text{ cm}^{-2}$	L $10^{38} \text{ erg s}^{-1}$	Notes
N III 4634-41	0.71 ± 0.05	0.42 ± 0.04	0.13 ± 0.01	WR
[Fe III] 4658	0.31 ± 0.02	0.12 ± 0.01	0.04	
He II 4686	2.78 ± 0.06	1.18 ± 0.03	0.35 ± 0.01	WR
[Ar IV] 4711	0.32 ± 0.02	0.14 ± 0.01	0.04	
[Ar IV] 4740	0.10 ± 0.01	0.04 ± 0.01	0.01	
H β	40.0 ± 0.1	15.9 ± 0.1	4.8 ± 0.1	
[O III] 4959	69.7 ± 0.2	26.8 ± 0.1	8.0 ± 0.1	
[Fe III] 4986	0.15 ± 0.01	0.06 ± 0.01	0.02	
[O III] 5007	213 ± 1	80.7 ± 0.4	24.1 ± 0.1	
He II 5412	0.07 ± 0.01	0.02	0.01	WR
[Cl III] 5518	0.22 ± 0.01	0.07 ± 0.01	0.02	
[Cl III] 5538	0.17 ± 0.01	0.06 ± 0.01	0.02	
[N II] 5755	0.06 ± 0.01	0.02	0.01	
C IV 5801-12	1.53 ± 0.08	0.47 ± 0.02	0.14 ± 0.01	WR
He I 5876	6.21 ± 0.02	1.87 ± 0.01	0.56 ± 0.01	
[O I] 6300	0.46 ± 0.02	0.13 ± 0.01	0.04	
[S III] 6312	0.89 ± 0.03	0.24 ± 0.01	0.07 ± 0.01	
[N II] 6548	1.49 ± 0.07	0.39 ± 0.02	0.12 ± 0.01	
H α	176 ± 1	45.7 ± 0.3	13.7 ± 0.1	
[N II] 6584	4.48 ± 0.20	1.16 ± 0.05	0.35 ± 0.01	
He I 6678	2.10 ± 0.01	0.53 ± 0.01	0.16 ± 0.01	
[S II] 6717	3.74 ± 0.01	0.94 ± 0.01	0.28 ± 0.01	
[S II] 6731	3.12 ± 0.01	0.78 ± 0.01	0.23 ± 0.01	
He I 7065	1.88 ± 0.01	0.44 ± 0.01	0.13 ± 0.01	
[Ar III] 7135	7.33 ± 0.01	1.71 ± 0.01	0.51 ± 0.01	
[S III] 9069	21.3 ± 0.2	3.82 ± 0.04	1.14 ± 0.01	

$T_e = 10,400^{+900}_{-700}$ K and [S III] 6312/9069 to obtain $T_e = 8300^{+70}_{-50}$ K. For reference, Peimbert (2003) obtained $N_e = 415 \pm 35 \text{ cm}^{-3}$ ([S II]) and $T_e = 10\,800 \pm 300$ K ([N II]).

We are unable to determine the oxygen abundance from the use of auroral T_e diagnostics ($\lambda 4363$ [O III] is not available to MUSE at zero redshift). Instead, we rely on strong line calibrations (Maiolino & Mannucci 2019), which are widely used for extragalactic H II regions for which direct temperature determinations are not feasible. The calibration of the N2 index (-1.59) by Marino et al. (2013) implies $12 + \log(O/H) = 8.01 \pm 0.32$, versus 7.90 ± 0.16 following Curti et al. (2017). The O3N2 index ($+2.3$) lies beyond the calibrated range of Marino et al. (2013), with $12 + \log(O/H) = 8.10 \pm 0.21$ obtained from Curti et al. (2017), values typical of the present-day Small Magellanic Cloud (SMC) rather than the LMC (Russell & Dopita 1990; Pagel et al. 1978). Use of the integrated 30 Dor nebular fluxes from Pellegrini et al. (2010) provides N2 and O3N2 indices of -1.42 and 2.09 , indicating $12+\log(O/H) = 8.10 \pm 0.16$ or 8.19 ± 0.21 , respectively, following the Curti et al. (2017) calibrations.

Contemporary baseline LMC abundances (Vink et al. 2023, Table 1) including $12 + \log(O/H) = 8.36$ correspond to a mass fraction of $Z=0.008$, although the directly determined gas phase oxygen abundance within 30 Doradus ranges from $12+\log(O/H) = 8.26$ (Vermeij & van der Hulst 2002) to 8.5 (Peimbert 2003). It is clear that standard strong line calibrations significantly underestimate the true oxygen content of NGC 2070, since these are sensitive to ionization parameter as well as abundance (Kewley & Dopita 2002). Consequently caution should be used when inferring metallicities of low-redshift star forming galaxies from diagnostics within the MUSE spectral

range (see Easeman et al. 2023). By way of a test, spectral synthesis calculations are made for both $Z=0.008$ (well matched to NGC 2070) and $Z=0.002$ (significantly lower than NGC 2070, albeit inferred from strong line methods).

3.2 Population synthesis

In order to estimate the age and mass of the starburst region consistent with MUSE observations, we have employed several widely used population synthesis packages. Age estimates from H α are relatively metallicity insensitive, but WR bumps and UV diagnostics are strongly metallicity-dependent. Starburst99 (v7.0.1, Leitherer et al. 1999, 2014) involves a $1 \times 10^5 M_\odot$ burst of star formation, an initial mass function (IMF) from Kroupa (2008) with an upper mass limit of $120 M_\odot$. Modern non-rotating and rotating Geneva evolutionary models at Solar ($Z=0.014$ Ekström et al. 2012) and SMC ($Z=0.002$ Georgy et al. 2013) metallicities are available⁵, with the full range of metallicities for historical models available with either standard (Schaller et al. 1992) or enhanced mass-loss (Meynet et al. 1994).

Starburst99 model atmospheres are obtained from either WM-Basic (O, Pauldrach et al. 2001) or PoWR (WR, Gräfener et al. 2002), with ionizing fluxes from Smith et al. (2002) and Leitherer et al. (2010) and empirical UV spectral templates drawn from either the Milky Way or Magellanic Clouds (Robert et al. 1993).

Observed rotational velocities (e.g. Ramírez-Agudelo et al. 2017; Sabín-Sanjulián et al. 2017) are intermediate between non-rotating and rapidly rotating models (40% critical), and evidence points to a higher mass limit than $120 M_\odot$ (Crowther et al. 2010; Brands et al. 2022).

We also make use of the latest CB19 grid of Charlot & Bruzual models (Bruzual & Charlot 2003; Plat et al. 2019) which employ non-rotating PARSEC stellar evolutionary tracks from Chen et al. (2015) calculated for a range of metallicities, synthetic hot luminous star templates from WM-Basic, TLUSTY (OB), PoWR (WR) (Sánchez et al. 2022) with integrated populations drawn from either a Salpeter, Kroupa or Chabrier IMF for stars up to $M_{\text{up}} = 100, 300$ or $600 M_\odot$ (Sánchez et al. 2022).

Crucially, binary evolution is neglected in both Starburst99 and Charlot & Bruzual models, despite observational evidence indicating a high fraction of close binaries amongst massive stars at the LMC metallicity (Sana et al. 2013). Therefore we also consider BPASS (v2.2.1, Eldridge et al. 2017; Stanway & Eldridge 2018) models incorporating binary evolution, a Kroupa IMF and an upper mass limit of $M_{\text{up}} = 100$ or $300 M_\odot$. Stellar atmosphere models incorporated into BPASS that are relevant for young populations are WM-Basic (O), PoWR (WR) and ATLAS (B).

The H α equivalent width is a sensitive indicator of age for a young star burst. We measure $W_\lambda(\text{H}\alpha) = 692 \pm 24 \text{ Å}$. We initially focus on $Z=0.002$ predictions from Starburst99 on the basis of the strong line calibrations, so adopt contemporary non-rotating models from Georgy et al. (2013). We obtain an age of 4.2 Myr, such that the H α luminosity (Table 3) corresponds to a stellar mass of $5.5 \times 10^4 M_\odot$. Broadly similar results are obtained for historical $Z=0.008$ models (Meynet et al. 1994) aside from a higher mass of $8.5 \times 10^4 M_\odot$. Comparable results are obtained from the H β equivalent width, $W_\lambda(\text{H}\beta) = 97 \pm 1 \text{ Å}$. Revised ages accounting for underlying absorption in H $\alpha - \beta$ are barely affected owing to the exceptionally strong Balmer emission.

⁵ $Z=0.008$ models appropriate for the LMC have only recently become available (Eggenberger et al. 2021)

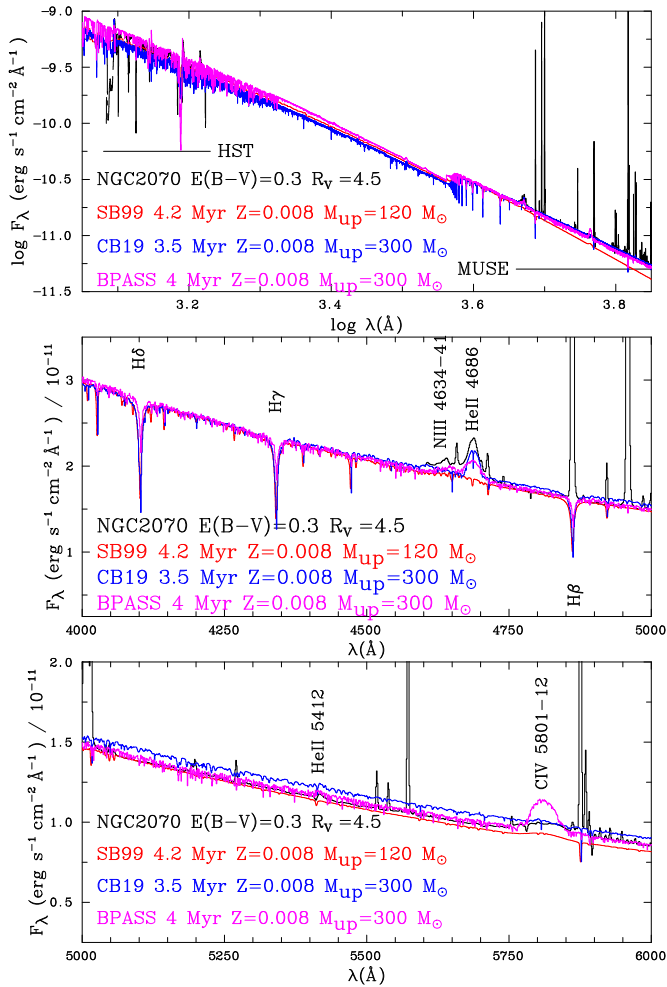


Figure 7. Top panel: Comparison between dereddened ($E_{B-V} = 0.3$, $R_V = 4.5$) integrated UV and MUSE spectrum of the central region of NGC 2070 (black) and the predicted 4.2 Myr Starburst99 spectra (red) based on $Z=0.008$ metallicity evolutionary models extending to $M_{up} = 120 M_\odot$ (Meynet et al. 1994), plus predicted 3.5 Myr CB19 spectra (blue) based on $Z=0.008$ metallicity evolutionary predictions (Chen et al. 2015) extending to $M_{up} = 300 M_\odot$ and predicted 4 Myr BPASS spectra (pink) also based on $Z=0.008$ predictions (Eldridge et al. 2017) for single stars extending to $M_{up} = 300 M_\odot$. Central panel: Zoom including blue WR bump (He II $\lambda 4686$ and N III $\lambda\lambda 4634-41$). A weak bump is predicted in the Starburst99 model, with improved agreement obtained from CB19 and BPASS models (similar WR emission is predicted for $M_{up} = 100 M_\odot$). Bottom panel: Zoom including yellow WR bump (C IV $\lambda\lambda 5801-12$). The 4.2 Myr Starburst99 model is a good match to the yellow bump, whereas this feature is too weak in CB19 and too strong in BPASS. Weak stellar He II $\lambda 5412$ is also observed in the MUSE dataset. Emission lines not explicitly labelled are nebular (H β , [O III] $\lambda 4959, 5007$, He I $\lambda 5876$).

In reality the stellar population within NGC 2070 is not coeval – see (Schneider et al. 2018b, their fig. 4) and (Castro et al. 2021b, their fig. 10). In particular the ages of OB stars within 1.2 arcmin of R136 (broadly comparable to MUSE pointing) span 1–7 Myr from comparison with evolutionary predictions for LMC metallicity OB stars (Brott et al. 2011), excluding the R136 star cluster whose age is ~ 1.5 Myr (Crowther et al. 2016; Brands et al. 2022). Nevertheless, the median age of massive stars in NGC 2070 (3.6 Myr, Schneider et al. 2018b) is in good agreement with the age inferred from H α using $Z=0.002$ or $Z=0.008$ metallicity models.

3.3 WR properties

The spectral resolution of MUSE prevents the detection of photospheric absorption lines, but the high S/N does reveal broad WR bumps (Fig. 2). The blue bump is dominated by broad He II $\lambda 4686$ (FWHM $\sim 25 \text{ \AA}$, $W_\lambda \sim 6 \text{ \AA}$), with no nebular component detected. Broad N III $\lambda\lambda 4634-41$ is also observed, suggesting a dominant late WN population, while the yellow WR bump is dominated by C IV $\lambda\lambda 5801-12$ (FWHM $\sim 80 \text{ \AA}$, $W_\lambda \sim 4 \text{ \AA}$) from WC stars. The high S/N of our MUSE integrated dataset unusually also permits broad He II $\lambda 5412$ emission to be detected. Optical emission line fluxes from individual stars are provided in Table 2 of Castro et al. (2018).

Both classical WR stars and main sequence very massive stars (WN5h and Of/WN) are major contributors to He II $\lambda 4686$, with R136a contributing $\sim 20\%$ of the total, whereas the blend of N III $\lambda\lambda 4634-41$ and C III $\lambda\lambda 4647-51$ and C IV $\lambda\lambda 5801-20$ are dominated by classical WR stars (primarily R140a). The presence of WR features in Starburst99, CB19 and BPASS synthetic spectroscopy provide independent age indicators (Schaerer & Vacca 1998). We require a non-standard extinction law in order to reconcile the UV and optical spectrophotometry of NGC 2070 with predictions. We adopt an LMC law with $R_V = 4.5$ (Mafz Apellániz et al. 2014; De Marchi & Panagia 2014; Brands et al. 2023), and obtain $E_{B-V} = 0.3$ mag ($A_V = 1.35$ mag) for spectral energy distribution comparisons in the top panel of Fig. 7. Masses inferred from Starburst99, CB19 and BPASS stellar continua are $7.7 \times 10^4 M_\odot$, $6.5 \times 10^4 M_\odot$ and $11 \times 10^4 M_\odot$, respectively, in reasonable agreement with $L(\text{H}\alpha)$ derived masses. The nebular continuum is not included in Fig. 7 since it has a negligible contribution to the far-UV and Paschen continua.

$Z=0.002$ metallicity models predict extremely weak WR emission for all population synthesis models. Consequently we adopt more realistic $Z=0.008$ models for age determinations based on WR stars, although different models have different time resolutions (e.g. 1 Myr intervals for BPASS). The peak strength of optical WR bumps occurs at 4.2 Myr, 3 Myr and 4 Myr for Starburst99, CB19 and BPASS models. Starburst99 models at solar metallicity ($Z=0.014$, Ekström et al. 2012), allow comparisons between peak WR ages associated with non-rotating (4.5 ± 0.5 Myr) and rotating (± 2 Myr) models.

We compare the Starburst99 synthetic spectrum associated with the 4.2 Myr age corresponding to the maximum WR population from the Meynet et al. (1994) evolutionary models in the central and bottom panels of Fig. 7, which coincide with the H α -inferred age. Both WR bumps are predicted, albeit significantly weaker than observed for the He II $\lambda 4686$ + N III $\lambda\lambda 4634-41$ bump. It is clear that either the number of WR stars predicted from single star models at low metallicity or their line luminosities, or both, are underestimated (stronger emission is predicted for solar metallicity models). The synthetic spectrum also highlights strong photospheric absorption lines associated with Balmer lines.

In contrast, the 3.5 Myr CB19 synthetic spectrum (blue) based on PARSEC evolutionary models at $Z=0.008$ with $M_{up} = 300 M_\odot$ (Chen et al. 2015) provides a stronger He II $\lambda 4686$ emission in the central panel of Fig. 7, albeit too weak and with negligible N III $\lambda\lambda 4634-41$ and C IV $\lambda\lambda 5801-12$ emission in lower panel. This age is close to the median 3.6 Myr age of massive stars in NGC 2070 according to Schneider et al. (2018b). Comparable WR emission is predicted at this age for CB19 models with $M_{up} = 100 M_\odot$, since very massive stars have somewhat shorter lifetimes.

For the BPASS single star models with $M_{up} = 300 M_\odot$, WR emission is most prominent at 4 Myr, with comparable C IV $\lambda\lambda 5801-12$ emission predicted (too strong), and a higher He II $\lambda 4686$ equivalent width, albeit comparable to predictions from CB19 models (central

and bottom panels of Fig. 7). The H α luminosity at this age for the $M_{\text{up}} = 300 M_{\odot}$ model corresponds to a stellar mass of $\sim 6 \times 10^4 M_{\odot}$.

Alternatively, it is possible to empirically estimate WR populations if line luminosity calibrations are available (Schaefer & Vacca 1998). Assuming the blue bump is dominated by WN stars, one obtains a population of ~ 20 WN6–8 stars (or 12 WN5–7h stars) based on the latest WR line luminosities at the LMC metallicity from Crowther et al. (2023). The yellow bump is dominated by WC stars, from which a population of 4 WC4–5 stars is obtained. In reality, WC stars also contribute 15% to the blue bump via C III $\lambda 4650$ and He II $\lambda 4686$. Consequently the inferred number of WN stars is reduced to 17 WN6–8 stars (or 10 WN5–7h stars). These calibrations are within a factor of two of the known population (11 WN stars, 2 WC4 including individual components of multiple WR systems R140a and Mk 34).

4 ANALYSIS OF INTEGRATED FAR-UV SPECTROSCOPY

In common with previous studies of young extragalactic stellar populations in the ultraviolet, we again utilise predictions of the emergent far-UV spectrum from the population synthesis tool Starburst99 (version 7.0.1, Leitherer et al. 1999, 2014), Charlot & Bruzual (CB19, Bruzual & Charlot 2003; Plat et al. 2019) and BPASS (v2.2.1, Eldridge et al. 2017; Stanway & Eldridge 2018) once our empirical dataset has been dereddened according to an LMC extinction law with $R_V = 4.5$ and $E_{B-V} = 0.3$ mag, as for the optical comparison. The $\lambda 1500$ luminosity of the NGC 2070 empirical dataset corresponds to $\log L_{\text{FUV}} = 38.04 \text{ erg s}^{-1}$.

Strong interstellar Ly α absorption impacts the observed N v $\lambda\lambda 1238$ –42 profile (e.g. Wofford et al. 2023, their fig. 3). We have estimated $\log N(\text{H I})/\text{cm}^2 = 21.75 \pm 0.05$ from Ly α fits to COS/G130M and STIS/E140M observations of individual stars within the MUSE field-of-view (Table C1). However, application to theoretical predictions leads to a suppressed continuum extending to $\sim 1300 \text{ \AA}$, contrary to observations. This is because LMC templates, which dominate the cumulative far-UV spectrum, span a broad range of $N(\text{H I})$ column densities (Welty et al. 2012). Consequently no corrections to Ly α have been applied, of relevance to detailed comparisons between observed and predicted N v $\lambda\lambda 1238$ –42 profiles.

Once again, although the optical strong line calibrations favour an unphysical SMC-like metallicity, we discuss both $Z=0.002$ and $Z=0.008$ metallicity predictions in the far-UV in order to test predictions. We limit our discussion to single bursts, although in reality NGC 2070 and other far-UV observations involve a mixed population. Dual or multiple age populations are occasionally implemented for spectral fitting (e.g. Chisholm et al. 2019; Sirressi et al. 2022), but NGC 2070 comprises a star cluster embedded within an extended (spatially and temporally) star forming region.

4.1 Starburst99

The primary age indicators in the far-UV are N v $\lambda\lambda 1238$ –42, Si IV $\lambda\lambda 1393$ –1402 and C IV $\lambda\lambda 1548$ –51 for metal-poor populations with Starburst99 since empirical LMC/SMC stellar libraries cutoff at $\lambda 1600$, preventing spectral comparisons for He II $\lambda 1640$, although predicted equivalent widths of several WR lines are available, including He II $\lambda 1640$. The maximum He II $\lambda 1640$ emission occurs at an age of 3.2 Myr for the $Z=0.002$ (Georgy et al. 2013) Starburst99 model. Fig. 8 provides a comparison between this model and dereddened NGC 2070 spectrum, revealing a good match to N v $\lambda\lambda 1238$ –42, a weak P Cygni C IV $\lambda\lambda 1548$ –51 profile, and a somewhat

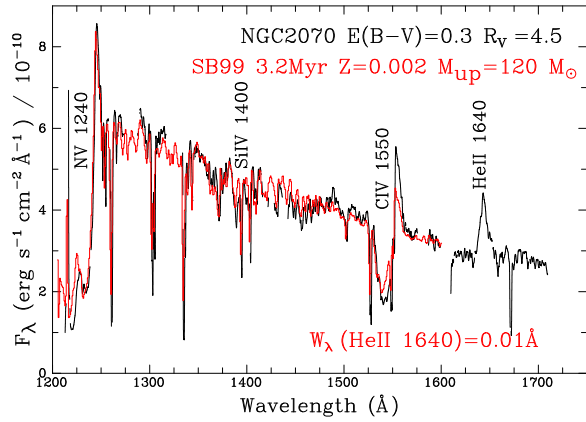


Figure 8. Comparison between dereddened ($E_{B-V} = 0.3$, $R_V = 4.5$) cumulative far-UV spectrum of the central region of NGC 2070 (black) and the predicted Starburst99 spectrum based on $Z=0.002$ evolutionary models (Georgy et al. 2013) with LMC/SMC UV templates at 3.2 Myr (red). Far-UV luminosities for this age correspond to stellar masses of $5 \times 10^4 M_{\odot}$. The cutoff at $\lambda 1600$ is due to the use of empirical templates (predicted He II $\lambda 1640$ emission equivalent width is indicated)

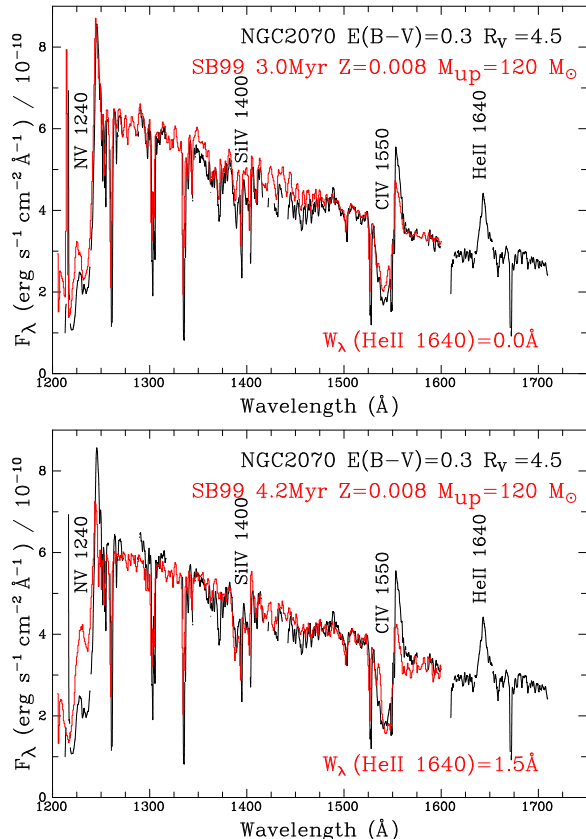


Figure 9. Comparison between dereddened ($E_{B-V} = 0.3$, $R_V = 4.5$) cumulative far-UV spectrum of the central region of NGC 2070 (black) and the predicted Starburst99 spectrum (red) based on $Z=0.008$ metallicity evolutionary models (Meynet et al. 1994) at 3.0 Myr (upper panel) and 4.2 Myr (lower panel) with LMC/SMC UV templates. Far-UV luminosities for this range of ages correspond to stellar masses of $5.5 - 8.5 \times 10^4 M_{\odot}$. The cutoff at $\lambda 1600$ is due to the use of empirical templates (predicted He II $\lambda 1640$ emission equivalent width is indicated).

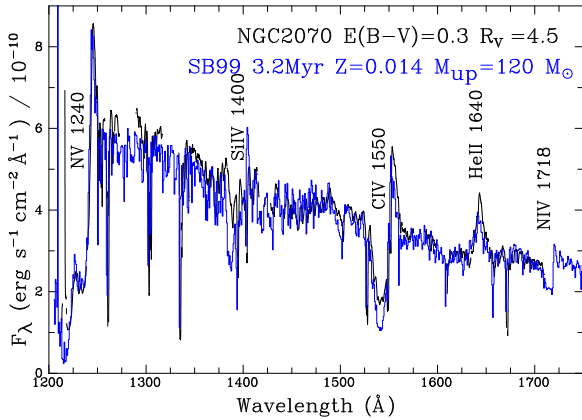


Figure 10. Comparison between dereddened ($E_{B-V} = 0.3$, $R_V = 4.5$) cumulative far-UV spectrum of the central region of NGC 2070 (black) and the predicted Starburst99 spectrum based on contemporary, non-rotating $Z=0.014$ evolutionary models (Ekström et al. 2012) plus empirical Milky Way UV templates at 3.2 Myr (blue). The Far-UV luminosity of this model corresponds to a stellar masses of $6 \times 10^4 M_\odot$.

too weak Si IV $\lambda\lambda 1393-1402$ wind signature. He II $\lambda 1640$ represents a major discrepancy, since the predicted emission of $W_\lambda = 0.01\text{\AA}$, is negligible with respect to the observed strength ($W_\lambda = 4.7 \pm 0.2\text{\AA}$).

In view of the overall poor match to observations at $Z=0.002$, in Fig. 9 we compare the dereddened NGC 2070 spectrum to predictions for non-rotating $Z=0.008$ metallicity models (Meynet et al. 1994) plus LMC/SMC empirical templates at 3 Myr (start of WR emission) and 4.2 Myr (peak WR emission). At 3 Myr results are broadly similar to the $Z=0.002$ case, whereas at 4.2 Myr (H α -inferred age from Section 3.2) the P Cygni Si IV $\lambda\lambda 1393-1402$ is well reproduced owing to OB supergiants being present in sizeable numbers, but the strength of both the N V $\lambda\lambda 1238-42$ and C IV $\lambda\lambda 1548-51$ P Cygni profiles are underpredicted. The He II $\lambda 1640$ emission strength remains underestimated, albeit with an improved predicted equivalent width of 1.5\AA .

Overall, metal poor Starburst99 models fare rather poorly in quantitatively reproducing the empirical dataset. The origin of this disagreement has multiple causes:

(i) The central region of NGC 2070 is not a coeval burst, since it hosts a young, potentially coeval, star cluster R136 contributing 1/3 of the far-UV continuum (Fig. 5) with the remainder spanning ages of 1–7 Myr (Schneider et al. 2018b). Improved agreement could be obtained by adopting dual age populations representing the cluster and extended star-forming region.

(ii) NGC 2070 is host to a number of VMS, within R136 and beyond, which possess very strong winds owing to their proximity to the Eddington limit (Bestenlehner 2020; Brands et al. 2022). These stars produce strong He II $\lambda 1640$ emission whilst on the main-sequence (Crowther et al. 2016). In addition we have shown that VMS contribute 18% of the far-UV continuum of NGC 2070, such that models with upper mass cutoffs at $\sim 100 M_\odot$ will underestimate the far-UV continuum. In order to reproduce He II $\lambda 1640$ in very young populations one needs to extend the IMF in population synthesis calculations to higher masses, and incorporate revised mass-loss prescriptions (Wofford et al. 2023).

(iii) The empirical UV template spectra at low metallicity in Starburst99 are a mix of SMC and LMC stars, since these were incorporated at a time prior to the availability of large numbers of high quality far-UV templates (Roman-Duval et al. 2020). OB stars in

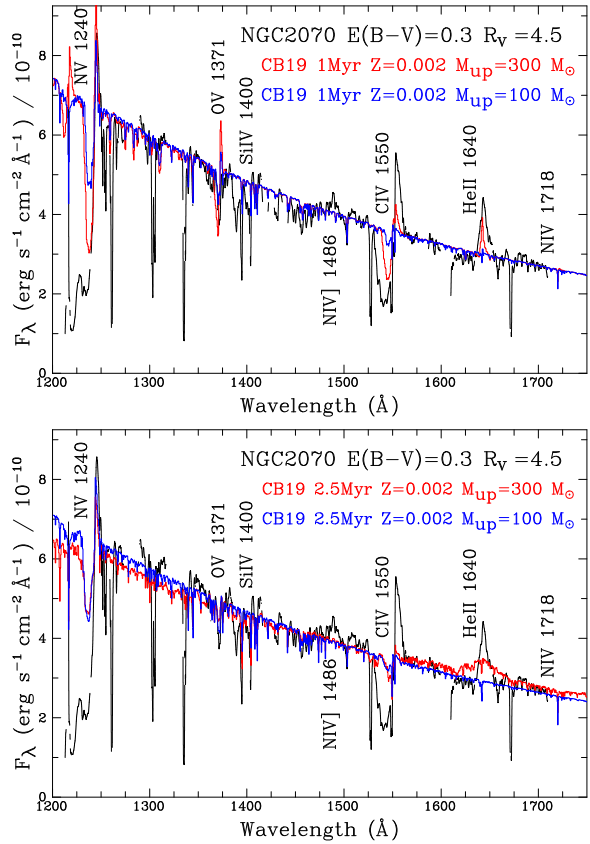


Figure 11. Comparison between dereddened ($E_{B-V} = 0.3$, $R_V = 4.5$) cumulative far-UV spectrum of the central region of NGC 2070 (black) and the predicted CB19 spectrum based on $Z=0.002$ evolutionary models (Chen et al. 2015) with $M_{up} = 300 M_\odot$ (red) or $100 M_\odot$ (blue) at 1.0 Myr (top panel) and 2.5 Myr (lower panel). Far-UV luminosities for this range of ages correspond to stellar masses of $5 - 8 \times 10^4 M_\odot$ for the $M_{up} = 300 M_\odot$ models.

the SMC possess significantly weaker winds than LMC counterparts (Prinja & Crowther 1998; Mokiem et al. 2007), so the use of SMC templates will yield weaker P Cygni profiles than observations at LMC composition. Alternatively theoretical spectra could lead to improved agreement (e.g. Leitherer et al. 2010), especially at low metallicities where empirical templates are scarce or unavailable.

(iv) It is well known that evolutionary models for single stars struggle to reproduce observed WR populations (Hamann et al. 2019). In reality, binary channels (including mergers) will increase the production of WR and lower mass He stars, which will enhance the strength of He II $\lambda 1640$ from all WR subtypes, as well as other far-UV P Cygni profiles (N V $\lambda\lambda 1238-42$ from WN stars, C IV $\lambda\lambda 1548-51$ from WC stars).

Previous analyses of extragalactic star clusters (e.g. Smith et al. 2016; Sirressi et al. 2022) or entire galaxies (e.g. James et al. 2014; Chisholm et al. 2019) are often more successful at reproducing far-UV observations than we have achieved for NGC 2070, albeit not universally so (Sidoli et al. 2006; Wofford et al. 2014; Leitherer et al. 2018). In part, this is achieved since the metallicity is varied, with high metallicities preferred in cases of strong stellar wind signatures, irrespective of nebular results for the regions in question.

To illustrate the role played by metallicity, we compare the dereddened UV spectrum of NGC 2070 with prediction of a 3.2 Myr model at $Z=0.014$ (Ekström et al. 2012) plus Milky Way UV templates in Fig. 10. In contrast to Fig. 9, N V $\lambda\lambda 1238-42$, C IV $\lambda\lambda 1548-51$ and

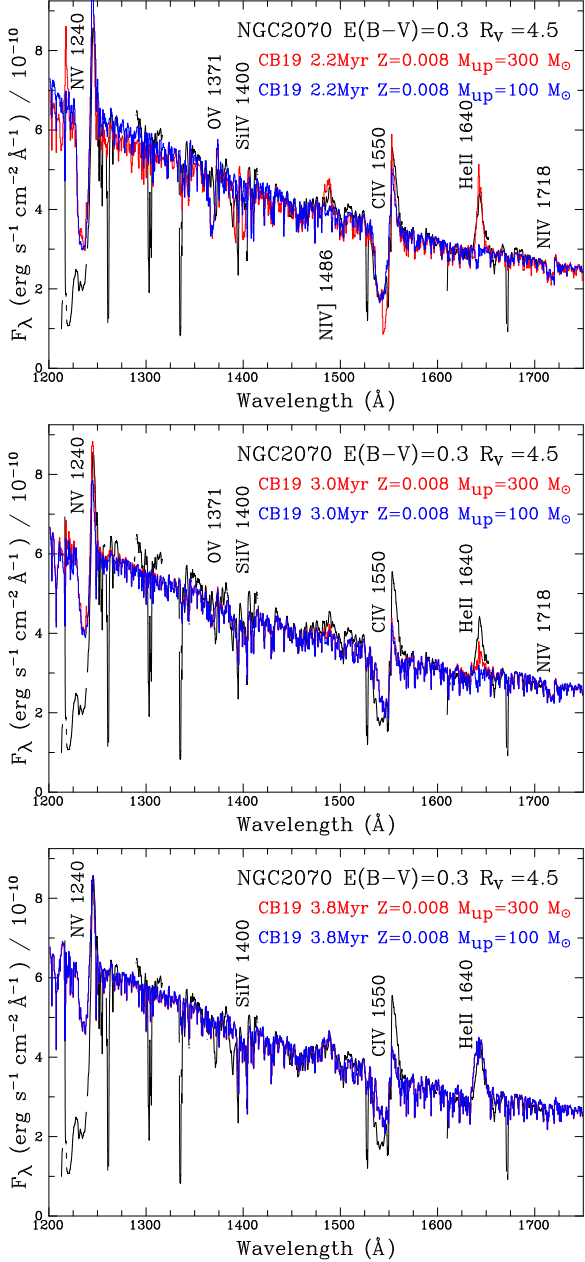


Figure 12. Comparison between dereddened ($E_{B-V} = 0.3$, $R_V = 4.5$) cumulative far-UV spectrum of the central region of NGC 2070 (black) and the predicted CB19 spectrum based on $Z=0.008$ evolutionary models (Chen et al. 2015) with $M_{up} = 300 M_\odot$ (red) or $100 M_\odot$ (blue) at 2.2 Myr (top panel), 3.0 Myr (central panel) and 3.8 Myr (lower panel). Far-UV luminosities for this range of ages correspond to stellar masses of $4 - 9 \times 10^4 M_\odot$ for the $M_{up} = 300 M_\odot$ models.

$\text{He II } \lambda 1640$ are now reasonably well predicted, with $\text{Si IV } \lambda\lambda 1393-1402$ a little too strong and the far-UV iron forest also over predicted. $\text{N IV } \lambda 1718$ is also prominent (recall Fig. 6), in contrast to metal poor predictions. Nevertheless, the overall match is satisfactory for an age close to the median of OB stars in NGC 2070 (Schneider et al. 2018b), albeit reliant on unphysical evolutionary models and templates.

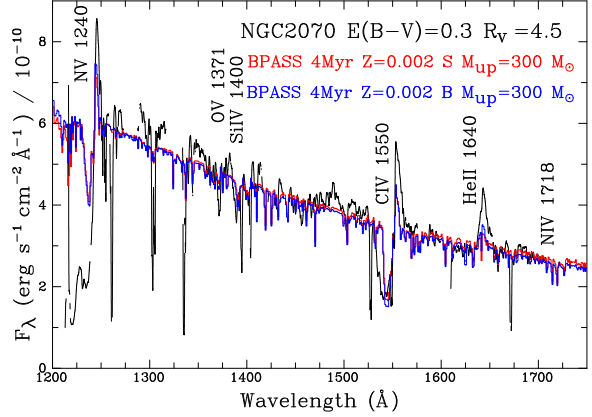


Figure 13. Comparison between dereddened ($E_{B-V} = 0.3$, $R_V = 4.5$) cumulative far-UV spectrum of the central region of NGC 2070 (black) and the predicted BPASS spectrum based on $Z=0.002$ metallicity evolutionary models (v.2.2.1 Eldridge et al. 2017) at 4 Myr for single stars (red) and binaries (blue). Far-UV luminosities correspond to stellar masses of $9 \times 10^4 M_\odot$ for the binary models.

4.2 Charlot & Bruzual

The extension of Charlot & Bruzual 2019 models to IMFs with high upper mass limits at a wide range of metallicities permits some deficiencies of current Starburst99 models to be addressed. As demonstrated by Wofford et al. (2023), the difference in predicted $\text{He II } \lambda 1640$ emission at ages of 1–3 Myr between $M_{up} = 100$ and $300 M_\odot$ at LMC metallicity ($Z=0.002$) is striking (their fig 4). This arises from the inclusion of mass-loss prescriptions for very massive stars (Vink et al. 2011). We compare far-UV CB19 ($Z=0.002$, Kroupa IMF) predictions for $M_{up} = 100$ and $300 M_\odot$ at 1.0 Myr and 2.5 Myr with NGC 2070 observations in Fig. 11. These ages correspond to the maximum $\text{He II } \lambda 1640$ emission due to very massive stars (1 Myr) and classical WR stars (2.5 Myr) for $M_{up} = 300 M_\odot$. At 1 Myr the high upper mass limit prediction provides a closer agreement with observations, albeit with $\text{O V } \lambda 1371$ too strong, $\text{He II } \lambda 1640$ too weak and $\text{C IV } \lambda\lambda 1548-51$ extremely weak. At 2.5 Myr, all wind features are far too weak, with the exception of $\text{He II } \lambda 1640$ for the $M_{up} = 300 M_\odot$ case which has a satisfactory emission equivalent width, albeit far broader than observed.

Consequently we also consider $Z=0.008$ predictions from CB19 with $M_{up} = 100$ and $300 M_\odot$. Fig. 12 compares predictions at 2.2, 3.0 and 3.8 Myr with observations, which span the range of ages at which prominent $\text{He II } \lambda 1640$ emission is predicted. At all ages the $M_{up} = 300 M_\odot$ model provides a better match to observations. Wofford et al. (2023, their fig. 4) highlight the sharp peak in $\text{He II } \lambda 1640$ at 2.2 Myr once very massive stars enter the late WN phase (see also Smith et al. 2023). Consequently the predicted $\text{He II } \lambda 1640$ is in good agreement with observations at this precise age, as is $\text{C IV } \lambda 1550$, albeit with $\text{O V } \lambda 1371$ over predicted, and $\text{Si IV } \lambda\lambda 1393-1402$ under predicted. $\text{N IV } \lambda 1486$ is observed in NGC 2070, though is overpredicted in models at this age that extend to $M_{up} = 300 M_\odot$.

Turning to later ages, $\text{O V } \lambda 1371$ has faded in strength after 3 Myr, with $\text{Si IV } \lambda\lambda 1393-1402$ now well reproduced, with $\text{He II } \lambda 1640$ emission a little too weak, with $\text{C IV } \lambda\lambda 1548-51$ also too weak, alongside $\text{Si IV } \lambda 1640$. $\text{C IV } \lambda\lambda 1548-51$ continues to weaken at later ages (3.8 Myr) with $\text{He II } \lambda 1640$ from classical WR stars now well reproduced and $\text{Si IV } \lambda\lambda 1393-1402$ still matched. Overall, use of CB19 models at $Z=0.008$ favour an age of 2.2 Myr for NGC 2070

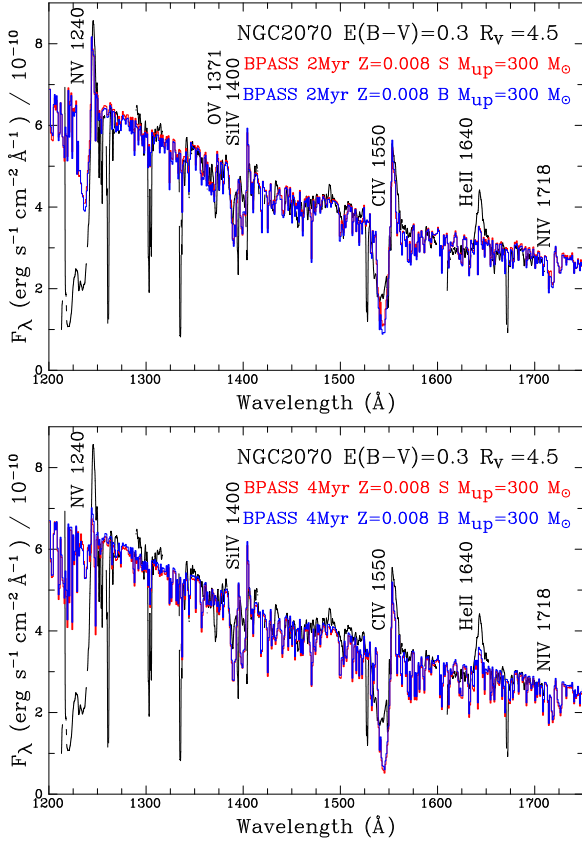


Figure 14. Comparison between dereddened ($E_{B-V} = 0.3$, $R_V = 4.5$) cumulative far-UV spectrum of the central region of NGC 2070 (black) and the predicted BPASS spectrum based on $Z=0.008$ metallicity evolutionary models (v.2.2.1 Eldridge et al. 2017) at 2 Myr (upper panel) and 4 Myr (lower panel) for single stars (red) and binaries (blue). Far-UV luminosities for this range of ages correspond to stellar masses of $5 - 9 \times 10^4 M_\odot$ for the binary models.

plus a high upper mass limit, in spite of the poor match to O v $\lambda 1371$ and very weak N iv $\lambda 1718$ (in contrast to *IUE* observations in Fig. 6).

4.3 BPASS

Finally, we consider BPASS (v.2.2.1 Eldridge et al. 2017; Stanway & Eldridge 2018) models for single or binary populations at $Z=0.002$ and $Z=0.008$, with a Kroupa IMF and $M_{\text{up}} = 300 M_\odot$. The maximum He ii $\lambda 1640$ emission at $Z=0.002$ is predicted at an age of 4 Myr (single or binary case), as shown in Fig. 13. At this metallicity all wind lines are predicted to be too weak, albeit with He ii $\lambda 1640$ only a factor of two weaker than observed, since several H-rich WN stars are predicted for cluster mass of $9 \times 10^4 M_\odot$ which reproduces the far-UV luminosity of NGC 2070. At $Z=0.008$, predictions are improved, as shown in Fig. 14 for ages of 2 Myr (upper panel) and 4 Myr (lower panel). For the 2 Myr case C iv $\lambda\lambda 1548-51$, N v $\lambda\lambda 1238-42$ and Si iv $\lambda\lambda 1393-1402$ are reasonably well reproduced, although He ii $\lambda 1640$ emission is only weakly present despite the inclusion of very massive stars, and N iv $\lambda 1718$ is very weak (in contrast with *IUE* observations in Fig. 6).

Binary models predict ~ 6 very massive stars at 2 Myr for a stellar mass of $5 \times 10^4 M_\odot$ that reproduces the far-UV luminosity of NGC 2070, categorized as a mix of O, Of and H-rich WN-types. In contrast with CB19 models, BPASS mass-loss prescriptions fail

to account for the proximity of very massive stars to the Eddington limit (Bestenlehner 2020; Brands et al. 2023). Predictions from single models are very similar to those from binary stars at such ages. At 4 Myr, preferred from predicted optical WR bumps, N v $\lambda\lambda 1238-42$ is now too weak, Si iv $\lambda\lambda 1393-1402$ is too strong, with He ii $\lambda 1640$ again too weak despite arising from classical WR stars. A stellar mass of $9 \times 10^4 M_\odot$ is required for the binary models to reproduce the far-UV luminosity of NGC 2070 at 4 Myr, with ~ 10 classical WR stars predicted (mix of WN and WC). Overall the 2 Myr BPASS models (single or binary) provide the closest match to UV observations, aside from the weakness of He ii $\lambda 1640$.

5 DISCUSSION AND CONCLUSIONS

We present the integrated VLT/MUSE spectrum of the central 2×2 arcmin 2 (30×30 pc 2) region of NGC 2070, the dominant giant H II region of the Tarantula (30 Doradus) region in the LMC, and construct an empirical far-UV spectrum of this region by combining observations of individual stars with templates from the ULLYSES survey (Roman-Duval et al. 2020). This region is unique in the sense that we are able to compare results from an individual treatment of stars with an integrated approach, plus both classical Wolf-Rayet stars and VMS have been identified within this region. A summary of UV and optical results is presented in Table 4.

Martins et al. (2023) consider UV and optical spectroscopic indicators of WR and very massive stars in nearby star-forming regions, favouring optical diagnostics to identify the latter. Neither the far-UV (HST) nor optical (MUSE) spectroscopy of NGC 2070 permit unique diagnostics of VMS since both populations have similar He ii $\lambda 1640$ morphologies (Fig. 4) and metal lines in the vicinity of He ii $\lambda 14686$ are dominated by classical WR stars (Fig. 2). Consequently, despite NGC 2070 having the richest VMS population in the Local Group, their presence is masked by its mixed age population, which includes classical WR stars. Nevertheless, unambiguous diagnostics of very young populations (required for VMS) exist in the optical (Martins et al. 2023) and far-UV (Crowther et al. 2016), the latter involving the presence of P Cygni O v $\lambda 1371$ and He ii $\lambda 1640$ emission with Si iv $\lambda\lambda 1393-1402$ absent.

If we were reliant solely on integrated visual spectroscopy of NGC 2070 we would substantially underestimate its metallicity from strong line diagnostics (Marino et al. 2013; Curti et al. 2017) but obtain an age of the stellar population (~ 4 Myr from Starburst99 and BPASS, 3.5 Myr from CB19) in close agreement with the median age of massive stars within the region. The Starburst99 inferred mass is broadly consistent with that of the star cluster R136 (Hunter et al. 1995; Andersen et al. 2009) which likely dominates the stellar mass of the region. The strength of WR bumps from historical LMC metallicity models (Meynet et al. 1994) implemented in Starburst99 are underestimated, although results from contemporary LMC models (Chen et al. 2015) plus a high $M_{\text{up}} = 300 M_\odot$ in CB19 and BPASS models are improved for He ii $\lambda 14686$ and C iv $\lambda\lambda 1580-12$. The number of WR stars estimated from line luminosities of blue and yellow WR bumps is in good agreement with latest empirical calibrations for LMC metallicity (Crowther et al. 2023).

Starburst99 predictions from $Z=0.008$ metallicity evolutionary models (Meynet et al. 1994) plus Magellanic Cloud empirical UV templates are incapable of reproducing the primary wind features in the integrated far-UV spectrum of NGC 2070 at a single age. For example, the maximum predicted emission $W_\lambda(\text{He ii } \lambda 1640) = 1.5 \text{ \AA}$, a factor of three lower than observed ($4.7 \pm 0.2 \text{ \AA}$). Starburst99 models using contemporary solar metallicity models (Ekström et al. 2012)

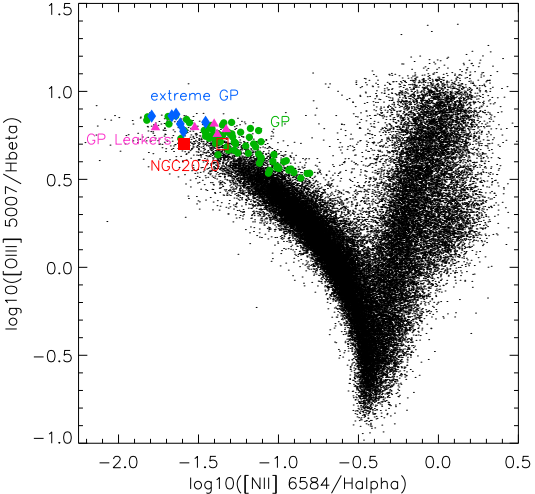


Figure 15. BPT diagram (Baldwin et al. 1981) illustrating the similarity in integrated strengths between NGC 2070/Tarantula (filled/open red square), Green Pea (green circles), extreme Green Pea (blue diamonds), and Lyman-continuum emitting Green Pea (pink triangles) galaxies, together with plus SDSS star-forming galaxies (black dots, Abazajian et al. 2009), adapted from Micheva et al. (2017, their fig.2) and Crowther et al. (2017).

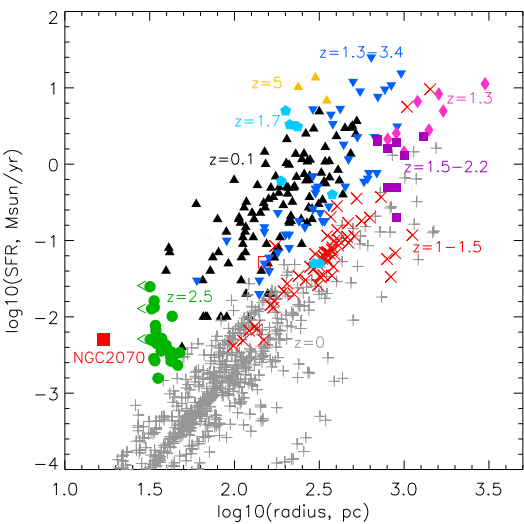


Figure 16. Comparison between the integrated star-formation rate of NGC 2070/Tarantula (filled/open red square) and star-forming knots from local star-forming galaxies ($z=0$, grey Kennicutt et al. 2003) to those at a range of redshifts ($z=0.1$ to 5), adapted from Johnson et al. (2017, their fig.2) and Crowther et al. (2017).

and Milky Way templates at 3.2 Myr provide a better match despite an unphysical metallicity. Various reasons for these deficiencies are set out in Section 4 including the mixed age of massive stars contributing to the integrated light (only 1/5 arises from the R136 cluster), plus the lack of high quality empirical templates (e.g. ULLYSES, Roman-Duval et al. 2020), neglect of very massive stars and the lack of binary evolutionary models.

CB19 models accounting for $Z=0.008$ evolutionary models (Chen et al. 2015) and synthetic spectra are more successful at reproducing $\text{He II } \lambda 1640$ emission at 2.2 Myr since they extend to higher initial masses $M_{\text{up}} = 300 M_{\odot}$) and fold in contemporary mass-loss prescriptions for very massive stars, although no single age provides a

Table 4. Summary of results for individual versus integrated treatment of NGC 2070 in ultraviolet and visual, with integrated results obtained from Starburst99 (SB99) using $Z=0.008$ evolutionary models (Meynet et al. 1994) and $M_{\text{up}} = 120 M_{\odot}$, Charlot & Bruzual (CB19) using $Z=0.008$ evolutionary models (Chen et al. 2015) and $M_{\text{up}} = 100$ or $300 M_{\odot}$ or BPASS $Z=0.008$ single and binary models (v.2.2.1 Eldridge et al. 2017; Stanway & Eldridge 2018). LMC WR template luminosities are from Crowther et al. (2023) while N2 and O3N2 strong line calibrations are from Curti et al. (2017).

Property	Individual	Ref	Integrated	This study
Visual (MUSE)				
Age (Myr)	1–7, 1–2.5†	a,b	4.2, 3.0, 4	SB99, CB19, BPASS
Mass ($10^5 M_{\odot}$)	0.5–1.0	c,d	0.85, 0.6, 1.1	SB99, CB19, BPASS
$M_{\text{up}} (M_{\odot})$	~270	b	100–300	CB19
N(WN)	11	e	10–17	WR templates
N(WC4)	2	e	4	WR templates
$\log(\text{O/H})+12$	8.26–8.5	f,g	7.9–8.1	N2, O3N2 diagnostics
Far-UV (HST)				
Age (Myr)	1.5†	h	4.2, 2.2, 2	SB99, CB19, BPASS
Mass ($10^5 M_{\odot}$)	0.85, 0.4, 0.5	SB99, CB19, BPASS
$M_{\text{up}} (M_{\odot})$	~250	h	300	CB19
Z	0.014	SB99‡

a: Schneider et al. (2018b); b: Brands et al. (2022); c: Hunter et al. (1995); d: Andersen et al. (2009); e: Doran et al. (2013); f: Vermeij & van der Hulst (2002); g: Peimbert (2003); h: Crowther et al. (2016)
‡ $Z=0.014$ models (Ekström et al. 2012) and Milky Way templates. † R136 cluster

satisfactory solution for all UV diagnostics. BPASS (Eldridge et al. 2017) models incorporate binary evolution, but do not currently incorporate enhanced mass-loss for very massive stars resulting from their proximity to the Eddington limit. Consequently BPASS models are unable to reproduce strong $\text{He II } \lambda 1640$ in metal poor models even with $M_{\text{up}} = 300 M_{\odot}$.

Fixing $Z=0.008$ and combining UV and optical spectroscopic diagnostics, Starburst99 models at ~ 4.2 Myr are capable of reproducing some optical ($\text{H}\alpha$, $\text{C IV } \lambda\lambda 15801-12$) and UV ($\text{Si IV } \lambda\lambda 1393-1402$) features of NGC 2070, although $\text{He II } \lambda 1640$, $\lambda 4686$ and $\text{C IV } \lambda\lambda 1548-51$ are too weak. CB19 models at 3.8 Myr provide a better match to $\text{He II } \lambda 1640$ and $\lambda 4686$, although $\text{C IV } \lambda\lambda 1548-51$ and $\lambda\lambda 15801-12$ are too weak, while BPASS models at 4 Myr underpredict $\text{He II } \lambda 1640$, $\lambda 4686$, overpredicts $\text{C IV } \lambda\lambda 15801-12$, with $\text{Si IV } \lambda\lambda 1393-1402$ and $\text{C IV } \lambda\lambda 1548-51$ broadly satisfactory. In view of our results, caution should be given to specific ages and metallicities of young, unresolved stellar populations (see Martins & Palacios 2022; Wofford et al. 2023). Should observed regions include multiple star clusters or clusters embedded within extended star-forming regions, it would be more realistic to incorporate either a dual or multiple populations (e.g. Chisholm et al. 2019; Sirressi et al. 2022), although the extended population of NGC 2070 is far from coeval (Schneider et al. 2018b).

Although NGC 2070 is located in the LMC, our nearest extragalactic star-forming galaxy, if one compares its nebular properties in the BPT diagram (Baldwin et al. 1981), it is located close to extreme Green Pea galaxies (Cardamone et al. 2009) as shown in Fig. 15. Green Pea galaxies have received considerable interest since a subset have been established as Lyman continuum leakers (Izotov et al. 2016). $\text{H}\alpha$ observations of NGC 2070 (Fig. 1) suggests a significant fraction of ionizing photons escape the region. By way of example, BPASS models at 4 Myr favour a stellar mass of $8.5 - 11 \times 10^4 M_{\odot}$ from FUV-optical continua, but only $6 \times 10^4 M_{\odot}$ from its $\text{H}\alpha$ luminosity, favouring a sizeable escape fraction of ionizing photons (see also Doran et al. 2013).

The relatively high star-formation rate of NGC 2070 for its size is

also more comparable to the properties of star-forming knots at high redshift with respect to local star-forming galaxies (Kennicutt et al. 2003), as shown in Fig. 16. Specifically, NGC 2070 properties are close to clumps in the lensed galaxy SDSS J1110+6459 at $z \sim 2.5$ (Johnson et al. 2017). Star-forming knots in the lensed Sunburst arc have a similar size to NGC 2070 but are significantly more intensive (Rivera-Thorsen et al. 2017, 2019; Vanzella et al. 2022).

As we have shown, the ULLYSES survey (Roman-Duval et al. 2020) provides high quality far-UV empirical templates for OB stars at half-solar metallicity, which serve as alternatives to widely used theoretical models (Leitherer et al. 2010) in population synthesis tools. High quality optical VLT/Shooter spectroscopy of ULLYSES targets has also been acquired (XshootU, Vink et al. 2023), which complement the present MUSE observations since templates achieve higher spectral resolution, extend to the violet and complement existing optical spectroscopic libraries of massive stars (e.g. Vero et al. 2022).

Indeed, ULLYSES/XshootU spectroscopy have been secured for a large number of OB stars in the SMC. Ideally we would wish to extend this study to the 1/5 solar metallicity of the SMC. The richest young star formation region in the SMC is NGC 346 (Massey et al. 1989). STIS/G140L spectroscopy has recently been obtained for the O stars within the central region of this giant H II region (Rickard et al. 2022), whose central 1×1 arcmin 2 (20×20 pc 2) has been observed with VLT/MUSE. Unfortunately, NGC 346 lacks a massive young star cluster at its heart such that any analysis would need to reflect stochasticity in both its star formation history and IMF (e.g. da Silva et al. 2014; Krumholz et al. 2015; Orozco-Duarte et al. 2022).

Nevertheless, there are other large star-forming complexes in the Magellanic Clouds (Evans et al. 2006), for which quantitative UV-optical analysis could be undertaken based on ULLYSES templates plus integral field observations from the upcoming SDSS-V Local Volume Mapper (LVM, Kollmeier et al. 2017).

ACKNOWLEDGEMENTS

This study has been made possible courtesy of: (i) Science Verification MUSE observations of NGC 2070 (proposal led by Jorge Melnick and Chris Evans); (ii) the Director's Discretionary ULLYSES survey, which was implemented by a Space Telescope Science Institute (STScI) team led by Julia Roman-Duval, having been recommended by the Hubble UV Legacy Science Definition Working Group chaired by Sally Oey, convened in 2018 by the then STScI Director Ken Sembach. Thanks to Linda Smith for providing useful comments on a draft version of the manuscript, and the referee for feedback which helped to improve the clarity of the paper.

Based on observations made with ESO telescopes at the Paranal observatory under programme ID 60.A-9351(A) and observations obtained with the NASA/ESA Hubble Space Telescope, retrieved from the Mikulski Archive for Space Telescopes (MAST) at the STScI. STScI is operated by the Association of Universities for Research in Astronomy, Inc. under NASA contract NAS 5-26555. PAC is supported by the Science and Technology Facilities Council research grant ST/V000853/1 (PI. V. Dhillon). NC gratefully acknowledges funding from the Deutsche Forschungsgemeinschaft (DFG) CA 255/1-1.

This research has made use of the SIMBAD database, operated at CDS, Strasbourg, France. Starlink software is currently supported by the East Asian Observatory. IRAF was distributed by the National Optical Astronomy Observatory, which was managed by the Association of Universities for Research in Astronomy (AURA) under a

cooperative agreement with the National Science Foundation. For the purpose of open access, the author has applied a Creative Commons Attribution (CC BY) license to any Author Accepted Manuscript version arising.

DATA AVAILABILITY

The integrated MUSE and far-UV spectroscopy of NGC 2070 are available in ascii format (wavelength in Å, flux in erg s $^{-1}$ cm $^{-2}$ Å $^{-1}$) at 10.5281/zenodo.10204404.

REFERENCES

- Abazajian K. N., et al., 2009, *ApJS*, **182**, 543
- Andersen M., Zinnecker H., Moneti A., McCaughrean M. J., Brandl B., Brandner W., Meylan G., Hunter D., 2009, *ApJ*, **707**, 1347
- Bacon R., et al., 2010, in McLean I. S., Ramsay S. K., Takami H., eds, Society of Photo-Optical Instrumentation Engineers (SPIE) Conference Series Vol. 7735, Ground-based and Airborne Instrumentation for Astronomy III. p. 773508 ([arXiv:2211.16795](https://arxiv.org/abs/2211.16795)), doi:10.1117/12.856027
- Baldwin J. A., Phillips M. M., Terlevich R., 1981, *PASP*, **93**, 5
- Bartzakos P., Moffat A. F. J., Niemela V. S., 2001, *MNRAS*, **324**, 18
- Berg D. A., et al., 2022, *ApJS*, **261**, 31
- Bestenlehner J. M., 2020, *MNRAS*, **493**, 3938
- Bestenlehner J. M., et al., 2014, *A&A*, **570**, A38
- Bestenlehner J. M., et al., 2020, *MNRAS*, **499**, 1918
- Bestenlehner J. M., Crowther P. A., Broos P. S., Pollock A. M. T., Townsley L. K., 2022, *MNRAS*, **510**, 6133
- Bosch G., Terlevich R., Melnick J., Selman F., 1999, *A&AS*, **137**, 21
- Brands S. A., et al., 2022, *A&A*, **663**, A36
- Brands S. A., de Koter A., Bestenlehner J. M., Crowther P. A., Kaper L., Caballero-Nieves S. M., Gräfener G., 2023, *A&A*, **673**, A132
- Brott I., et al., 2011, *A&A*, **530**, A115
- Bruzual G., Charlot S., 2003, *MNRAS*, **344**, 1000
- Cardamone C., et al., 2009, *MNRAS*, **399**, 1191
- Carnall A. C., et al., 2023, *MNRAS*, **518**, L45
- Castro N., Crowther P. A., Evans C. J., Mackey J., Castro-Rodriguez N., Vink J. S., Melnick J., Selman F., 2018, *A&A*, **614**, A147
- Castro N., et al., 2021a, *The Messenger*, **182**, 50
- Castro N., et al., 2021b, *A&A*, **648**, A65
- Chandar R., Leitherer C., Tremonti C. A., 2004, *ApJ*, **604**, 153
- Chen Y., Bressan A., Girardi L., Marigo P., Kong X., Lanza A., 2015, *MNRAS*, **452**, 1068
- Chisholm J., Rigby J. R., Bayliss M., Berg D. A., Dahle H., Gladders M., Sharon K., 2019, *ApJ*, **882**, 182
- Crowther P. A., 2019, *Galaxies*, **7**, 88
- Crowther P. A., 2022, arXiv e-prints, p. arXiv:2207.08690
- Crowther P. A., Dessart L., 1998, *MNRAS*, **296**, 622
- Crowther P. A., Smith L. J., 1997, *A&A*, **320**, 500
- Crowther P. A., Walborn N. R., 2011, *MNRAS*, **416**, 1311
- Crowther P. A., Schnurr O., Hirschi R., Yusof N., Parker R. J., Goodwin S. P., Kassim H. A., 2010, *MNRAS*, **408**, 731
- Crowther P. A., et al., 2016, *MNRAS*, **458**, 624
- Crowther P. A., Castro N., Evans C. J., Vink J. S., Melnick J., Selman F., 2017, *The Messenger*, **170**, 40
- Crowther P. A., Broos P. S., Townsley L. K., Pollock A. M. T., Tehrani K. A., Gagné M., 2022, *MNRAS*, **515**, 4130
- Crowther P. A., Rate G., Bestenlehner J. M., 2023, *MNRAS*, **521**, 585
- Curti M., Cresci G., Mannucci F., Marconi A., Maiolino R., Esposito S., 2017, *MNRAS*, **465**, 1384
- Curtis-Lake E., et al., 2023, *Nature Astronomy*, **7**, 622
- da Silva R. L., Fumagalli M., Krumholz M. R., 2014, *MNRAS*, **444**, 3275
- de Koter A., Heap S. R., Hubeny I., 1997, *ApJ*, **477**, 792
- de Koter A., Heap S. R., Hubeny I., 1998, *ApJ*, **509**, 879
- De Marchi G., Panagia N., 2014, *MNRAS*, **445**, 93

- De Marchi G., et al., 2011, *ApJ*, **739**, 27
- Doran E. I., et al., 2013, *A&A*, **558**, A134
- Easeman B., Schady P., Wuyts S., Yates R., 2023, *MNRAS*, arXiv:2311.03514
- Eggenberger P., et al., 2021, *A&A*, **652**, A137
- Ekström S., et al., 2012, *A&A*, **537**, A146
- Eldridge J. J., Stanway E. R., Xiao L., McClelland L. A. S., Taylor G., Ng M., Greis S. M. L., Bray J. C., 2017, *Publ. Astron. Soc. Australia*, **34**, e058
- Evans C. J., Lennon D. J., Smartt S. J., Trundle C., 2006, *A&A*, **456**, 623
- Evans C. J., et al., 2011, *A&A*, **530**, A108
- Evans C. J., et al., 2015, *A&A*, **574**, A13
- Fahrion K., De Marchi G., 2023, *arXiv e-prints*, arXiv:2311.06336
- Feast M. W., Thackeray A. D., Wesselink A. J., 1960, *MNRAS*, **121**, 337
- Fitzpatrick E. L., Savage B. D., 1984, *ApJ*, **279**, 578
- Georgy C., et al., 2013, *A&A*, **558**, A103
- Gräfener G., Koesterke L., Hamann W. R., 2002, *A&A*, **387**, 244
- Hamann W. R., et al., 2019, *A&A*, **625**, A57
- Heap S. R., Ebbets D., Malumuth E., 1992, in European Southern Observatory Conference and Workshop Proceedings. p. 347
- Hénault-Brunet V., et al., 2012, *A&A*, **546**, A73
- Hillier D. J., Miller D. L., 1998, *ApJ*, **496**, 407
- Howarth I. D., 1983, *MNRAS*, **203**, 301
- Howarth I. D., Murray J., Mills D., Berry D. S., 2004, Starlink User Note, **50**
- Hunter D. A., Shaya E. J., Holtzman J. A., Light R. M., O'Neil Earl J. J., Lynds R., 1995, *ApJ*, **448**, 179
- Izotov Y. I., Schaerer D., Thuan T. X., Worseck G., Guseva N. G., Orlitová I., Verhamme A., 2016, *MNRAS*, **461**, 3683
- James B. L., Aloisi A., Heckman T., Sohn S. T., Wolfe M. A., 2014, *ApJ*, **795**, 109
- Johnson T. L., et al., 2017, *ApJ*, **843**, L21
- Kalari V. M., Horch E. P., Salinas R., Vink J. S., Andersen M., Bestenlehner J. M., Rubio M., 2022, *ApJ*, **935**, 162
- Keenan F. P., Aller L. H., Ryans R. S. I., Hyung S., 2001, *Proceedings of the National Academy of Science*, **98**, 9476
- Kennicutt R. C. Jr., 1998, *ARA&A*, **36**, 189
- Kennicutt R. C. Jr., Bresolin F., Bomans D. J., Bothun G. D., Thompson I. B., 1995, *AJ*, **109**, 594
- Kennicutt R. C. Jr., et al., 2003, *PASP*, **115**, 928
- Kewley L. J., Dopita M. A., 2002, *ApJS*, **142**, 35
- Kollmeier J. A., et al., 2017, *arXiv e-prints*, p. arXiv:1711.03234
- Kroupa P., 2008, in Knapen J. H., Mahoney T. J., Vazdekis A., eds, Astronomical Society of the Pacific Conference Series Vol. 390, Pathways Through an Eclectic Universe. p. 3 (arXiv:0708.1164), doi:10.48550/arXiv.0708.1164
- Krumholz M. R., Fumagalli M., da Silva R. L., Rendahl T., Parra J., 2015, *MNRAS*, **452**, 1447
- Lanz T., Hubeny I., 2007, *ApJS*, **169**, 83
- Leitherer C., et al., 1999, *ApJS*, **123**, 3
- Leitherer C., Ortiz Otálvaro P. A., Bresolin F., Kudritzki R.-P., Lo Faro B., Pauldach A. W. A., Pettini M., Rix S. A., 2010, *ApJS*, **189**, 309
- Leitherer C., Ekström S., Meynet G., Schaerer D., Agienko K. B., Levesque E. M., 2014, *ApJS*, **212**, 14
- Leitherer C., Byler N., Lee J. C., Levesque E. M., 2018, *ApJ*, **865**, 55
- Maiolino R., Mannucci F., 2019, *A&ARv*, **27**, 3
- Maíz Apellániz J., et al., 2014, *A&A*, **564**, A63
- Marino R. A., et al., 2013, *A&A*, **559**, A114
- Martins F., Palacios A., 2022, *A&A*, **659**, A163
- Martins F., Schaerer D., Marques-Chaves R., Upadhyaya A., 2023, *A&A*, **678**, A159
- Massey P., Hunter D. A., 1998, *ApJ*, **493**, 180
- Massey P., Parker J. W., Garmany C. D., 1989, *AJ*, **98**, 1305
- Massey P., Penny L. R., Vukovich J., 2002, *ApJ*, **565**, 982
- Massey P., Puls J., Pauldach A. W. A., Bresolin F., Kudritzki R. P., Simon T., 2005, *ApJ*, **627**, 477
- Massey P., Morrell N. I., Neugent K. F., Penny L. R., DeGioia-Eastwood K., Gies D. R., 2012, *ApJ*, **748**, 96
- Melnick J., 1985, *A&A*, **153**, 235
- Meynet G., Maeder A., Schaller G., Schaerer D., Charbonnel C., 1994, *A&AS*, **103**, 97
- Micheva G., Oey M. S., Jaskot A. E., James B. L., 2017, *ApJ*, **845**, 165
- Mokiem M. R., et al., 2007, *A&A*, **473**, 603
- Orozco-Duarte R., et al., 2022, *MNRAS*, **509**, 522
- Pagel B. E. J., Edmunds M. G., Fosbury R. A. E., Webster B. L., 1978, *MNRAS*, **184**, 569
- Parker J. W., 1993, *AJ*, **106**, 560
- Pauldach A. W. A., Hoffmann T. L., Lennon M., 2001, *A&A*, **375**, 161
- Peimbert A., 2003, *ApJ*, **584**, 735
- Pellegrini E. W., Baldwin J. A., Ferland G. J., 2010, *ApJS*, **191**, 160
- Pellegrini E. W., Baldwin J. A., Ferland G. J., 2011, *ApJ*, **738**, 34
- Plat A., Charlot S., Bruzual G., Feltre A., Vidal-García A., Morisset C., Chevallard J., Todt H., 2019, *MNRAS*, **490**, 978
- Prinja R. K., Crowther P. A., 1998, *MNRAS*, **300**, 828
- Ramírez-Agudelo O. H., et al., 2017, *A&A*, **600**, A81
- Rickard M. J., et al., 2022, *A&A*, **666**, A189
- Rivera-Thorsen T. E., et al., 2017, *A&A*, **608**, L4
- Rivera-Thorsen T. E., et al., 2019, *Science*, **366**, 738
- Robert C., Leitherer C., Heckman T. M., 1993, *ApJ*, **418**, 749
- Roman-Duval J., et al., 2020, *Research Notes of the American Astronomical Society*, **4**, 205
- Russell S. C., Dopita M. A., 1990, *ApJS*, **74**, 93
- Sabbi E., et al., 2013, *AJ*, **146**, 53
- Sabbi E., et al., 2016, *ApJS*, **222**, 11
- Sabín-Sanjulián C., et al., 2017, *A&A*, **601**, A79
- Sana H., et al., 2013, *A&A*, **550**, A107
- Sánchez S. F., et al., 2022, *ApJS*, **262**, 36
- Saxena A., et al., 2020, *A&A*, **636**, A47
- Schaerer D., Vacca W. D., 1998, *ApJ*, **497**, 618
- Schaller G., Schaerer D., Meynet G., Maeder A., 1992, *A&AS*, **96**, 269
- Schneider F. R. N., et al., 2018a, *Science*, **359**, 69
- Schneider F. R. N., et al., 2018b, *A&A*, **618**, A73
- Selman F., Melnick J., Bosch G., Terlevich R., 1999, *A&A*, **341**, 98
- Shenar T., et al., 2017, *A&A*, **598**, A85
- Shenar T., et al., 2019, *A&A*, **627**, A151
- Shenar T., et al., 2022, *A&A*, **665**, A148
- Sidoli F., Smith L. J., Crowther P. A., 2006, *MNRAS*, **370**, 799
- Sirressi M., et al., 2022, *AJ*, **164**, 208
- Smith L. J., Norris R. P. F., Crowther P. A., 2002, *MNRAS*, **337**, 1309
- Smith L. J., Crowther P. A., Calzetti D., Sidoli F., 2016, *ApJ*, **823**, 38
- Smith L. J., et al., 2023, *arXiv e-prints*, arXiv:2310.03413
- Stanway E. R., Eldridge J. J., 2018, *MNRAS*, **479**, 75
- Steidel C. C., Strom A. L., Pettini M., Rudie G. C., Reddy N. A., Trainor R. F., 2016, *ApJ*, **826**, 159
- Tehrani K. A., Crowther P. A., Bestenlehner J. M., Littlefair S. P., Pollock A. M. T., Parker R. J., Schnurr O., 2019, *MNRAS*, **484**, 2692
- Vacca W. D., Robert C., Leitherer C., Conti P. S., 1995, *ApJ*, **444**, 647
- Vanzella E., et al., 2022, *A&A*, **659**, A2
- Vermeij R., van der Hulst J. M., 2002, *A&A*, **391**, 1081
- Verro K., et al., 2022, *A&A*, **661**, A50
- Vink J. S., Muijres L. E., Anthonisse B., de Koter A., Gräfener G., Langer N., 2011, *A&A*, **531**, A132
- Vink J. S., et al., 2023, *A&A*, **675**, A154
- Walborn N. R., Blades J. C., 1997, *ApJS*, **112**, 457
- Walborn N. R., et al., 2014, *A&A*, **564**, A40
- Welty D. E., Xue R., Wong T., 2012, *ApJ*, **745**, 173
- Wofford A., Leitherer C., Salzer J., 2013, *ApJ*, **765**, 118
- Wofford A., Leitherer C., Chandar R., Bouret J.-C., 2014, *ApJ*, **781**, 122
- Wofford A., et al., 2023, *MNRAS*, **523**, 3949
- Wong T., et al., 2022, *ApJ*, **932**, 47

APPENDIX A: TEMPLATE UV SPECTRA

The NGC 2070 far-ultraviolet spectrum has been constructed from a combination of empirical spectra (of individual stars) and use of template OB stars (Table A1) and Of/WN and WR stars (Table A2 for the remainder, primarily drawn from Data Release 6 (DR6) of the ULL-YSES survey (Roman-Duval et al. 2020). Figures A1–A4 present cumulative far-UV spectra for O, Of/WN, WR and B stars, respectively, including breakdowns between empirical datasets and templates (separated into supergiants and non-supergiants for B stars).

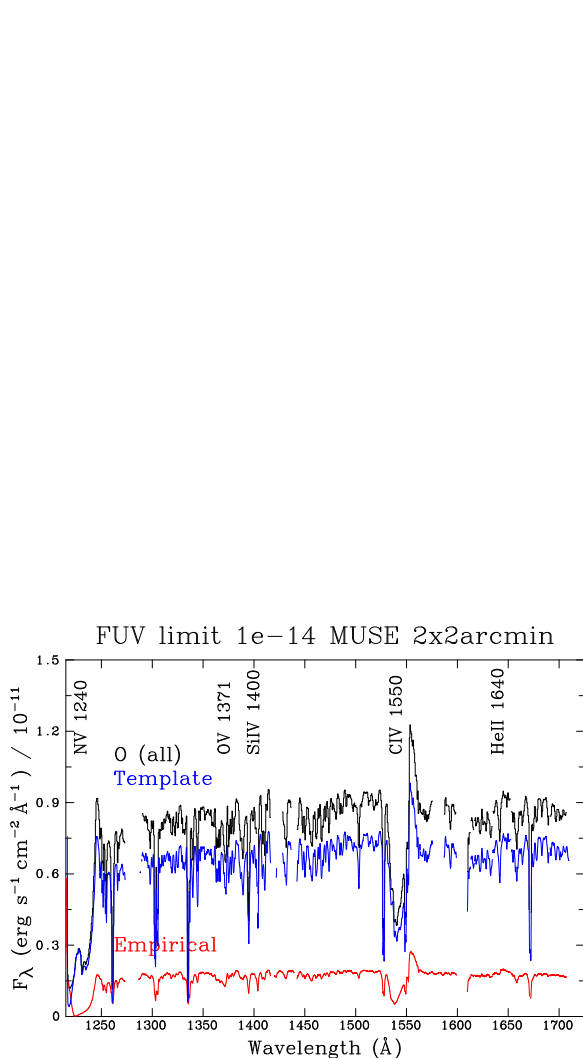


Figure A1. Cumulative O-type far-UV spectrum of the central region of NGC 2070 (black) based on empirical data of 34 individual stars (red) and 159 LMC template stars (blue). Gaps in spectra arise from incomplete spectral coverage (e.g. COS G130M+G160M).

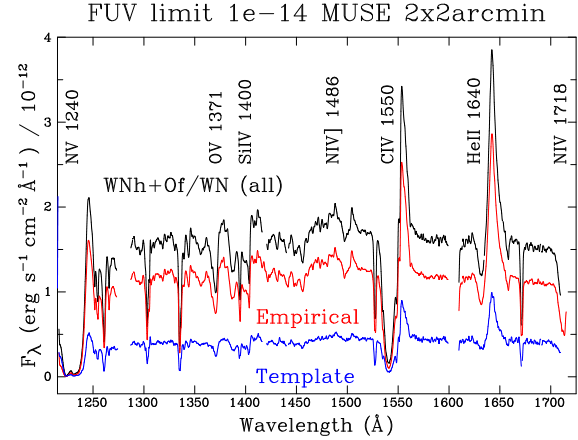


Figure A2. Cumulative WNh+Of/WN far-UV spectrum of the central region of NGC 2070 (black) based on empirical data of 7 individual stars (red) and 5 LMC template stars (blue). Gaps in spectra arise from incomplete spectral coverage (e.g. COS G130M+G160M).

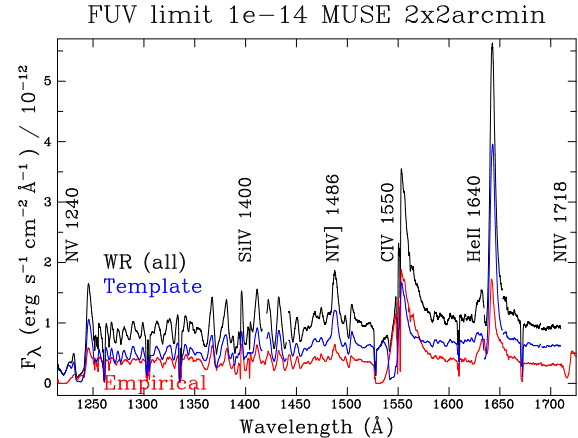


Figure A3. Cumulative WR far-UV spectrum of the central region of NGC 2070 (black) based on empirical data of R140a1 (red, WN+WC) and 5 LMC template stars (blue, 4 WN, 1 WC).

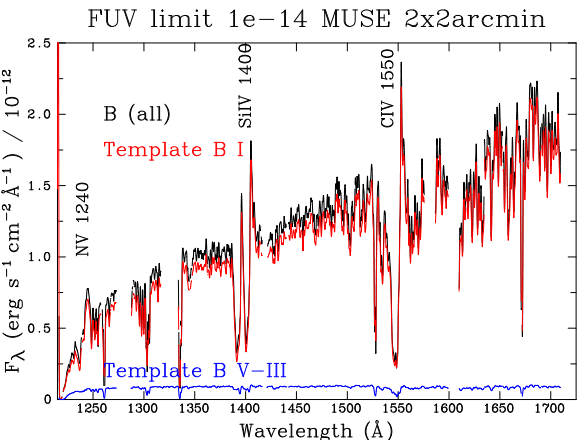


Figure A4. Cumulative B-type far-UV spectrum of the central region of NGC 2070 (black) based on LMC templates for 10 supergiants (red) and 6 non-supergiants (blue). Gaps in spectra arise from incomplete spectral coverage (e.g. COS G130M+G160M).

Table A1. LMC template UV spectra of normal OB stars from HST ULLYSES survey (Roman-Duval et al. 2020). COS gratings G130M+G160M are abbreviated as G1#0M.

Template	— Dwarf —		— Giant —		— Supergiant —	
	Star (Sp Type)	Instrument/Grating	Star (Sp Type)	Instrument/Grating	Star (Sp Type)	Instrument/Grating
O2	BI 237 (O2 V)	COS G1#0M	VFTS 72 (O2 V-III)	COS G1#0M	Mk 42 (O2 If*)	STIS/E140M
O2.5	VFTS 169 (O2.5 V)	COS G1#0M	N11 ELS 26 (O2.5 III)	COS G1#0M
O3	N11 ELS 60 (O3 V)	COS G1#0M	VFTS 267 (O3 III-I)	COS G1#0M	VFTS 180 (O3 If*)	STIS E140M
O3.5	VFTS 404 (O3.5: V:)	COS G1#0M
O4	W61 28-5 (O4 V)	COS G1#0M	Sk -67° 69 (O4 III)	STIS E140M	Sk -67° 166 (O4 I)	STIS E140M
O4.5	Sk -70° 60 (O4-5 V)	STIS E140M
O5	PGMW 3120 (O5.5 V)	STIS E140M	N11 ELS 38 (O5 III)	COS G1#0M	[ST92] 4-18 (O5 If)	COS G1#0M
O6	PGMW 3070 (O6 V)	STIS E140M	Sk -71° 19 (O6 III)	COS G1#0M	Sk -67° 111 (O6 Ifa)	STIS E140M
O6.5	Sk -71° 50 (O6.5 III)	STIS E140M
O7	Sk -67° 118 (O7 V)	STIS E140M	BI 272 (O7 II)	STIS E140M	Sk -69° 83 (O7.5 If)	STIS E140M
O8	BI 184 (O8 V)	COS G1#0M	Sk -67° 101 (O8 II)	STIS E140M	PGMW 1363 (O8.5 If)	STIS E140M
O9	VFTS 66 (O9 V)	COS G1#0M	Sk -71° 8 (O9 II)	STIS E140M	Sk -67° 107 (O9 Ib)	STIS E140M
O9.5	Sk -66° 17 (O9.5 II)	COS G1#0M	Sk -67° 5 (O9.7 Ib)	STIS E140M
B0	HV 5622 (B0 V)	COS G1#0M	Sk -70° 79 (B0 III)	STIS E140M	Sk -68° 52 (B0 Ia)	STIS E140M
B0.5	Sk -67° 216 (B0.5 V)	STIS E140M	Sk -68° 155 (B0.5 I)	COS G1#0M
B0.7	Sk -68° 140 (B0.7 Ib-Iab)	COS G1#0M
B1	Sk -65° 2 (B1 V)	STIS E140M	Sk -71° 35 (B1 II)	COS G1#0M	Sk -66° 35 (BC1 Ia)	COS G1#0M
B1.5	Sk -67° 14 (B1.5 Ia)	STIS E140M
B2	Sk -68° 26 (BC2 Ia)	COS G1#0M
B9	Sk -67° 207 (B9 Ia)	COS G1#0M

Table A2. LMC template UV spectra of normal Of/WN and WR stars from HST ULLYSES survey (Roman-Duval et al. 2020) except where noted

Template	Star (Sp Type)	Instrument/Grating
O2 If/WN5	Sk -67° 22 (O2 If/WN5)	STIS/E140M
O2.5 If/WN6	Mk 39 (O2.5 If/WN6)	COS G130M+G160M
O3.5 If/WN7	Mk 51 (O3.5 If/WN7)	COS G140L ^c
O4 If/WN8	R136b (O4 If/WN8)	GHRS G140L ^a
WN5h	R136a3 (WN5h)	GHRS G140L ^b
WN6	Sk -71° 21 (WN6h)	STIS E140M
WN7-8	VFTS 108 (WN7h)	COS G140L ^c
WC4	Sk -69° 191 (WC4)	STIS E140M

a: de Koter et al. (1998), b: de Koter et al. (1997); c: GO 15629 (Mahy)

APPENDIX B: CENSUS OF FAR-UV BRIGHTEST SOURCES OF NGC 2070

Table B1 lists stars of known spectral type within the MUSE footprint, sorted by far-UV flux, based on a calibration of F275W or F336W photometry drawn from HTTP (Sabbi et al. 2013, 2016). HSH95-17 is included since it lies within R136 GHRS/G140L 2×2 arcsec 2 region and is considered to be an early O star (Kalari et al. 2022), although a few other sources exceeding $F_{1500} \geq 10^{-14}$ erg s $^{-1}$ cm $^{-2}$ Å $^{-1}$ have been excluded since their spectral types are unknown. These include HSH95-76 (P 870, $m_{\text{F275W}} = 13.57$ mag, Sabbi et al. (2016)), SMB 136 ($m_{\text{F275W}} = 13.88$ mag, Sabbi et al. (2016)), HSH95-87 ($m_{\text{F336W}} = 14.27$ mag, Sabbi et al. (2016)), HSH95 120 ($m_{\text{F275W}} = 14.55$ mag, Sabbi et al. (2016)), HSH95-139 ($m_{\text{F336W}} = 14.80$ mag, Hunter et al. (1995)), HSH95-129 ($m_{\text{F336W}} = 14.97$ mag, Hunter et al. (1995)).

Table B2 lists stars of known spectral type beyond the MUSE footprint but within the 3×3 arcmin 2 region sampled with *IUE/SWP* (Vacca et al. 1995), sorted by far-UV flux, based on a calibration of F275W or F336W photometry drawn from HTTP (Sabbi et al. 2013, 2016). Bright sources lacking spectral types include SMB-183 ($m_{\text{F275W}} = 14.11$ mag, Sabbi et al. (2016)), SMB-196 ($m_{\text{F275W}} = 14.27$ mag, Sabbi et al. (2016)) and SMB-245 ($m_{\text{F275W}} = 14.67$ mag, Sabbi et al. (2016)).

Table B1. Stars within the NGC 2070 MUSE field of view, sorted by far-UV flux (F_{1500} units of $\text{erg s}^{-1} \text{cm}^{-2} \text{\AA}^{-1}$), either measured from spectroscopy or estimated from photometry, primarily drawn from HTTP (Sabbia et al. 2013, 2016), the latter indicated in parentheses. Catalogues include R (Feast et al. 1960), Mk (Melnick 1985), P (Parker 1993), HSH (Hunter et al. 1995), SMB (Selman et al. 1999), VFTS (Evans et al. 2011) and CCE (Castro et al. 2018). Spectra used in our integrated far-UV spectrum of NGC 2070 are of individual sources or templates with the exception of GHRS/G140L spectroscopy of the central 2×2 arcsec of R136a (indicated with \ddagger) while several templates are adjusted to measured STIS/G140L flux levels from Massey et al. (2005, indicated with \dagger). Further details of far-UV templates are provided in Tables A1–A2. Sources considered to be very massive stars (VMS, $\geq 100 M_\odot$) from spectroscopy analyses (Bestenlehner et al. 2014; Tehrani et al. 2019; Brands et al. 2022) are indicated with \checkmark . COS gratings G130M+G160M are abbreviated as G1#OM.

R	Mk	P	HSH	SMB	VFTS	CCE	SpT	Ref	HTTP	m_{275W} mag	m_{F336W} mag	m_{F555W} mag	Ref	F_{1500} 10^{-13}	Spectrum (Template)	Ref	VMS
140a	...	877	...	6	507	3191	WC4+WN6+	Do13	053841.601-690513.43	10.97	11.28	12.20	S	3.72	STIS/E140M	1	...
136a1	3	7	WN5h	CD98	11.20	12.28	D	(3.32)	GHRS/G140L \ddagger	4	\checkmark
140b	...	880	...	8	509	3174	WN5(h)+O	Ev11	053841.613-690515.17	11.09	11.43	12.47	S	(3.04)	(WN6)
...	42	922	2	10	...	2102	O2 If	CW11	053842.104-690555.29	11.08	11.51	12.82	S	3.01	STIS/E140M	3	\checkmark
136a2	5	WN5h	CD98	11.33	12.34	D	(2.93)	GHRS/G140L \ddagger	4	\checkmark
...	39	767	7	14	482	2003	O2.5 If/WN6+	Cr22	053840.214-690559.86	11.38	11.66	12.95	S	2.74	COS/G1#OM	3	\checkmark
142	...	987	1	3	533	2912	B1.5 Ia $^+$	Ev15	053842.738-690542.57	10.84	11.13	11.79	S	(2.50)	(B1.5I)
134	...	786	4	...	1001	1978	WN6(h)	CS97	053840.539-690557.18	11.45	11.62	12.70	S	(2.18)	(WN6)
137	...	548	...	5	431	2889	B1.5 Ia	Ev15	053836.959-690507.84	11.04	11.30	12.08	S	(2.08)	(B1.5I)
...	25	871	...	19	506	2395	ON2 V	Wa14	053841.545-690519.43	11.74	12.01	13.32	S	2.04	COS/G1#OM	3	\checkmark
141	...	1253	...	9	590	2190	B0.7 Iab	Ev15	053845.579-690547.80	11.42	11.60	12.58	S	(1.92)	(B0.7I)
136a3	6	WN5h	CD98	11.82	12.97	D	(1.87)	GHRS/G140L \ddagger	4	\checkmark
...	30	1018	15	24	542	2999	O2 If/WN5	CW11	053843.080-690546.86	11.91	12.22	13.48	S	1.85	COS/G1#OM	3	...
...	12	1257	...	11	591	1279	B0.2 Ia	Ev15	053845.687-690622.49	...	11.68	12.56	S	(1.80)	(B0I)
...	35	1029	12	23	545	1474	O2 If/WN5	CW11	053843.202-690614.44	11.93	12.23	13.46	S	(1.40)	(O2 I/WN5)	...	\checkmark
...	32	1130	13	21	1034	3043	O7.5 II	WB97	053844.192-690547.06	11.96	12.23	13.40	S	(1.37)	(O8 III)
...	34	1134	8	17	...	1766	WN5h+WN5h	Te19	053844.252-690605.93	12.04	12.11	13.15	S	(1.28)	(WN5)	...	\checkmark
138	...	499	...	4	424	...	B9 I+p	Ev15	053836.132-690558.01	...	11.50	11.79	S	(1.25)	(B9I)
...	37Wa	917	11	25	1021	1349	O4 If $^+$	MH98	053842.072-690614.32	12.16	12.35	13.36	S	(1.14)	(O4I)	...	\checkmark
...	11	1500	...	15	641	762	B0.5: I	Ev15	053849.723-690642.95	...	12.19	13.18	S	(1.13)	(B0.5I)
...	35Sa	1036	23	37	1028	1423	O4–5 V	WB97	053843.263-690616.51	12.18	12.53	13.85	S	(1.12)	(O4.5 V)
...	...	1080	25	39	1031	2186	O3–4 V	Bo99	053843.684-690547.89	12.20	12.56	14.23	S	(1.10)	(O3 V)
...	13	1311	...	40	599	1433	O3 III	Wa14	053846.177-690617.39	12.28	12.63	13.85	S	(1.02)	(O3 III)
...	26	1150	...	32	562	2819	O4 III	WB97	053844.406-690536.22	12.28	12.46	13.70	S	(1.02)	(O4 III)
136a5	20	O2 If	Cr16	12.49	13.71	D	(1.01)	GHRS/G140L \ddagger	4	\checkmark
136c	...	998	10	27	1025	1737	WN5h+?	Cr10	12.54	13.43	D	(0.97)	(WN5)	...	\checkmark
...	47	607	...	29	440	2417	O6–6.5 III	Wa14	053837.729-690521.03	12.15	12.44	13.69	S	0.96	STIS/E140M	2	...
...	33Na	1140	16	33	...	1943	OC2.5 If+O4 V	Br22	053844.329-690554.66	12.37	12.55	13.64	S	(0.94)	(O3I)
...	54	488	...	16	420	1689	B0.5 Ia	Ev15	053835.941-690609.23	12.20	12.26	13.10	S	(0.93)	(B0.5I)
...	27	850	...	38	502	2653	O9.7 II	Wa14	053841.271-690532.44	12.39	12.67	13.82	S	(0.92)	(O9.5 III)
...	...	1014	...	41	...	3062	O8:	Ca21	053843.030-690540.44	12.43	12.57	13.60	S	(0.89)	(O8 III)
136a7	24	20	O3 III(f*)	Be20	12.64	13.97	S	(0.88)	GHRS/G140L \ddagger	4	\checkmark
...	...	860	28	53	...	1912	O3 V	MH98	053841.490-690556.90	12.45	12.80	14.04	S	(0.87)	(O3 V)
...	...	1231	...	31	585	2193	O7 V	Wa14	053845.279-690546.53	...	12.66	13.78	S	(0.87)	(O7 V)
136b	...	985	9	18	...	1669	O4 If/WN8	Cr16	12.27	13.24	D	0.86	GHRS/G140L	5	\checkmark
...	37a	949	14	28	1022	1442	O3.5 If/WN7	CW11	053842.397-690615.08	12.33	12.48	13.52	S	0.82 \dagger	(O3.5 If/WN7)	6	\checkmark
...	24	1260	...	47	...	2760	O3 V	WB97	053845.687-690539.02	12.53	12.73	13.96	S	(0.81)	(O3 V)
140c	...	908	...	55	519	3112	O3–4((f))+OB	Wa14	053841.934-690513.02	12.53	12.81	14.18	S	(0.81)	(O3.5 V)
...	...	863	29	56	1014	1956:	O3 V	MH98	053841.507-690600.92	12.55	12.90	14.18	S	(0.80)	(O3 V)
...	33Sa	1120	18	44	...	2177	O3 III	Ma15	053844.123-690556.63	12.48	12.76	13.81	S	0.79 \dagger	(O3 III)	6	...
...	50	643	...	34	450	1293	O9.7 III:+O7::	Wa14	053838.476-690621.96	12.57	12.75	13.69	S	(0.78)	(O9.5 III)
136a4	21	O3 V	Be20	12.81	13.96	H	(0.75)	GHRS/G140L \ddagger	4	\checkmark
...	...	923	33	60	...	1793	O3 V	Ma05	053842.119-690600.73	...	13.09	14.33	S	0.75 \dagger	(O3 V)	6	...
136a6 #1	19	O2 I(n)f*p+?	Be20	12.86	13.92	H	(0.72)	GHRS/G140L \ddagger	4	...
...	49	691	...	30	...	1261	WN6(h)	CS97	053839.143-690621.24	12.66	12.62	13.41	S	(0.71)	(WN6)
136a6 #2	26	O2 I(n)f*p+?	Be20	12.89	14.19	H	(0.70)	GHRS/G140L \ddagger	4	...
...	...	912	38	70	1019	1608	O3 V+O6 V	Ma02	053842.004-690607.56	12.72	13.02	14.30	S	(0.68)	(O3 V)
...	6	1563	...	61	656	1979	O7.5 IIIp	Wa14	053851.200-690559.28	12.73	13.11	14.36	S	(0.68)	(O7 III)
...	8	1531	...	58	648	2780	O5.5 IV	Wa14	053850.400-690538.17	12.73	12.96	14.23	S	(0.67)	(O5.5 V)
...	38	930	...	45	525	1184	B0 Ia	Wa14	053842.209-690625.56	12.55	12.79	13.83	S	(0.67)	(B0I)
136a8	27	O2–3 V	Cr16	12.93	14.22	H	(0.67)	GHRS/G140L \ddagger	4	...
...	...	17	O	Ka22	13.00	13.78	H	(0.63)	GHRS/G140L \ddagger	4	...
...	...	1273	...	59	...	1223	O7:	Ca21	053845.842-690620.83	12.82	13.05	14.05	S	(0.62)	(O7 III)
...	30	O6.5 Vz	Be20	13.02	14.21	D	(0.62)	GHRS/G140L \ddagger	4	...
...	...	31	35	O2 V	Be20	053842.471-690604.53	...	12.89	14.05	S	0.61 \dagger	(O2 V)

Table B1. (continued)

R	Mk	P	HSH	SMB	VFTS	CCE	SpT	Ref	HTTP	m_{275W}	m_{336W}	m_{555W}	Ref	F_{1500}	Spectrum	Ref	VMS
										mag	mag	mag		10^{-13}	(Template)		
...	...	713	...	72	...	2245	O5 V	Bo99	053839.478-690510.36	12.85	13.20	14.60	S	(0.60)	(O4.5 V)
...	...	36	O2 If	Be20	13.06	14.41	S	(0.59)	(O2 I)	...	✓
...	...	35	O3 V	Be20	13.12	14.43	D	0.55†	GHRS/G140L‡	4	...
...	...	975	...	71	...	2748	O6–7 V	Bo99	053842.616-690536.74	12.93	13.18	14.50	S	(0.56)	(O6 V)
...	15	1312	...	43	...	2165	O7 V	WB97	053846.158-690551.37	...	13.14	14.13	S	(0.55)	(O7 V)
...	...	1113	53	78	1032	2977	O8 III	Le21	053844.063-690544.82	12.97	13.32	14.63	S	(0.54)	(O8 III)
140d	81	497	2231	O3.5 Vz+OB	Wa14	053841.126-690513.17	12.97	13.28	14.65	S	(0.54)	(O3.5 V)
...	...	42	O3 V+O3 V	Ma02	053842.119-690600.73	12.98	13.34	14.71	S,D	(0.54)	(O3 V)
...	...	75	O6 V	Be20	053842.178-690601.90	13.01	13.86	15.08	S,D	(0.52)	(O6 V)
...	...	288	...	84	385	2451	O4–5V	Wa14	053832.293-690523.85	13.22	13.38	14.65	S	0.51	COS/G140L	2	...
...	33Nb	1152	32	66	...	1896	O6.5 V	Be20	053844.467-690555.50	13.03	13.28	14.36	S	(0.51)	(O6 V)
...	...	1034	61	85	1027	2987	O5 V	Le21	053843.195-690542.61	13.05	13.38	14.68	S	(0.50)	(O4.5 V)
...	...	39	...	1005	...	O3 V+O5.5 V	Ma02	13.26	14.50	D	(0.50)	(O3 V)	
...	53	51	427	389	WN8(h)	Ev11	053836.407-690657.48	...	13.27	13.77	S	(0.49)	(WN7–8)
...	35N	1013	41	76	1026	1494	O3 III(f*)	MH98	053843.075-690611.28	...	13.29	13.97	S,D	(0.48)	(O3 III)
...	...	1042	56	87	1029	2128	O3.5I+OB	Wa14	053843.343-690547.55	13.10	13.39	14.71	S,D	(0.48)	(O3 I)
...	...	40	O3 V	Be20	13.30	14.56	D	(0.48)	(O3 V)
...	...	1195	43	83	...	2112	O3 V	MH98	053844.950-690554.11	13.12	13.37	14.57	S	(0.47)	(O3 V)
...	...	1123	...	74	1033	2913	O7 III	Le21	053844.172-690542.17	13.13	13.42	14.53	S	(0.46)	(O7 III)
...	...	885	...	68	512	1199	O2 V–III	Wa14	053841.734-690625.01	13.15	13.30	14.34	S	(0.46)	(O2 V)
...	51	666	...	50	457	603	O3.5If/WN7	CW11	053838.838-690649.49	...	12.98	13.81	S	0.45	COS/G140L	2	✓
...	...	724	...	75	...	1274	O7 III	Bo99	053839.692-690624.01	13.17	13.37	14.41	S	(0.45)	(O7 III)
...	14S	1350	...	64	608	1827	O4 III	Wa14	053846.785-690603.10	13.01	13.19	14.29	S	0.43	COS/G140L	2	...
...	...	723	...	92	...	2570	O5:	Ca21	053839.638-690526.37	13.21	13.53	14.77	S	(0.43)	(O5 III)
...	36	706	...	86	468	1749	O2 V	Wa14	053839.369-690606.49	13.21	13.39	14.58	S	(0.43)	(O2 V)
...	...	812	51	89	O3 V	MH98	053840.895-690555.93	13.23	13.48	14.70	S	(0.43)	(O3 V)
...	27E	858	...	100	503	...	O9 III	Wa14	053841.367-690532.44	13.23	13.57	14.87	S,D	(0.43)	(O9 III)
...	...	1267	...	90	...	2911	O7: V	Pa93	053845.757-690540.82	13.24	13.52	14.72	S	(0.42)	(O7 V)
...	28	805	...	80	...	2447	O5–6 V	Bo99	053840.798-690525.10	13.24	13.40	14.61	S	(0.42)	(O5.5 V)
...	...	787	...	103	...	2233	O9–B0 V	Bo99	053850.435-690534.56	13.25	13.60	14.98	S	(0.42)	(O9 V)
...	4	1607	...	65	664	774	O7 II	Wa14	053852.724-690643.13	...	13.37	14.38	S	0.41	COS/G140L	2	...
...	...	52	O3–4 Vz	Be20	13.46	14.72	D	(0.41)	GHRS/G140L‡	4	...
...	...	45	O4: Vz	Be20	13.48	13.65	D	(0.40)	(O4 V)
...	...	900	37	77	1018	1459	O2–4.5	He12	053841.874-690612.52	13.29	13.42	14.49	D	(0.40)	(O3 III)
...	...	49	O3 V	Be20	13.49	14.75	D	(0.40)	(O3 V)
...	...	50	O3–4 V	Be20	13.51	14.65	D	(0.39)	GHRS/G140L‡	4	...
...	...	55	O2 Vz	Be20	13.52	14.74	D	(0.39)	(O2 V)
...	5	1552	...	54	652	1405	B2 Ip+O9III:	Wa14	053851.043-690620.40	...	13.06	14.15	S	(0.39)	(B2 I)
...	...	46	O2–3 III	Be20	13.53	14.56	S	(0.39)	(O2.5 III)
...	...	506	...	82	...	1632	O8:	Ca21	053836.237-690608.42	13.35	13.52	14.55	S	(0.38)	(O8 III)
...	14N	1317	...	91	601	1890	O5–6 V	Wa14	053846.280-690559.32	13.36	13.56	14.68	S	(0.38)	(O5.5 V)
...	7	1553	...	94	651	2057	O7 V	Wa14	053851.029-690554.70	13.36	13.59	14.74	S	(0.38)	(O7 V)
...	...	47	111	O2 V	Be20	053842.630-690601.92	13.39	13.66	14.72	S	(0.37)	(O2 V)
...	...	48	O2–3 III	Be20	13.60	14.75	D	(0.36)	(O2.5 III)
...	...	58	O2–3 V	Be20	13.61	14.80	D	(0.36)	GHRS/G140L‡	4	...
...	...	467	...	93	416	1700	O8.5 V	Ma12	053835.570-690606.65	13.41	13.57	14.74	S	(0.36)	(O8 V)
...	106	583	2107	O8 V+O8.5 V	Wa14	053845.211-690548.48	13.44	13.71	14.92	S	(0.35)	(O8 V)
...	...	62	O2–3 V	Be20	13.65	14.91	D	(0.35)	GHRS/G140L‡	4	...
...	52	493	...	48	423	660	B1 Ia	Ev15	053836.053-690646.50	...	13.19	13.64	S	(0.34)	(B1 I)
...	...	1340	...	110	604	2884	O8.5 V	Wa14	053846.567-690537.10	13.47	13.71	14.95	S	(0.34)	(O8 V)
...	...	1248	...	112	...	3034	O6:	Ca21	053845.494-690543.99	13.48	13.73	15.00	S	(0.34)	(O6 III)
...	...	1614	...	118	667	1699	O6 V	Wa14	053852.832-690612.01	...	13.95	15.08	S	0.33	COS/G140L	2	...
...	...	86	O5: V	Be20	13.72	14.73	D	(0.33)	GHRS/G140L‡	4	...
...	...	827	60	95	1007	1763	O6.5 V–III	He12	053841.066-690601.89	...	13.72	14.86	S,D	(0.32)	(O6.5 III)
...	...	67	96	...	1857:	...	O6:	Ca21	053841.324-690557.59	13.52	13.86	15.09	S,D	(0.32)	(O6 III)
...	...	661	...	108	455	1572	O5:V:n	Wa14	053838.759-690613.22	13.55	13.75	15.08	S	(0.32)	(O4.5 V)
...	...	1281	...	114	...	2033	O7:	Ca21	053845.907-690550.77	13.56	13.76	14.90	S	(0.31)	(O7 III)
...	37Wb	897	44	88	1017	1374	O2 If/WN5	CW11	053841.862-690614.41	13.56	13.60	14.53	S	(0.31)	(O2 If/WN5)	...	✓
...	...	761	63	105	...	2077	O3–6 V	WB97	053840.143-690551.26	13.56	13.76	14.86	S	(0.31)	(O4.5 V)
...	...	781	72	113	...	1974	O6:	Ca21	053840.477-690553.42	13.57	13.83	14.99	S	(0.31)	(O6 III)

Table B1. (continued)

R	Mk	P	HSH	SMB	VFTS	CCE	SpT	Ref	HTTP	m_{275W}	m_{F336W}	m_{F555W}	Ref	F_{1500}	Spectrum	Ref	VMS
										mag	mag	mag		10^{-13}	(Template)		
...	70	O5 Vz	Be20	13.81	14.96	D	(0.30)	GHRS/G140L‡	4	...
...	74	121	O6 V	MH98	13.82	15.11	D	(0.30)	(O6 V)
...	...	1329	...	122	...	2718	O9:	Ca21	053849.107-690547.18	13.63	13.86	15.23	S	(0.29)	(O9 III)
...	...	1023	59	99	...	1703	O3 III	MH98	053843.168-690603.65	13.63	13.73	14.76	S,D	(0.29)	(O3 III)
...	...	974	...	104	532	963	O3 V(n)z+OB	Wa14	053842.657-690635.83	...	13.85	14.81	S	(0.29)	(O3 V)
...	...	978	54	109	...	1963	O4:	Ca21	053842.679-690556.30	13.67	13.80	14.79	S	(0.28)	(O4 III)
...	...	71	O2–3 V	Be20	053842.365-690604.90	13.70	13.98	15.16	S,D	(0.28)	(O2.5 V)
...	...	57	O3 III(f*)	MH98	13.90	14.80	D	(0.28)	(O3 III)
...	...	776	...	124	484	3081	O6–7 V	Wa14	053840.354-690543.79	13.71	13.94	15.09	D	(0.27)	(O6 V)
...	...	921	82	134	522	3030	O6 II-lab+O5.5 V	Wa14	053842.082-690545.47	13.72	14.01	15.26	S	(0.27)	(O6 III)
...	...	77	O5.5 V+O5.5 V	Ma02	13.94	15.21	D	(0.27)	(O5.5 V)
...	...	1196	...	130	...	2763	O6:	Ca21	053844.958-690538.63	13.75	13.89	15.14	S	(0.26)	(O6 III)
...	...	80	O8 V	Be20	13.95	15.17	D	(0.26)	(O8 V)
...	...	973	...	129	...	2545	O8:	Ca21	053842.607-690522.21	13.75	14.05	15.25	S	(0.26)	(O8 III)
...	...	66	O2 V-III	Be20	13.95	15.06	D	(0.26)	GHRS/G140L‡	4	...
...	33Sb	1111	34	WC5	MH98	053844.062-690555.64	13.76	13.82	14.49	S	(0.26)	(WC4)
...	...	600	...	123	...	2946	O3–5 V	Bo99	053837.658-690542.06	...	13.96	15.04	S	(0.26)	(O4 V)
...	15S	1306	...	117	...	2053	O8 III	WB97	053846.113-690554.44	13.79	13.93	14.95	S	(0.25)	(O8 III)
...	...	89	O4 V	Cr16	13.99	14.76	D	(0.25)	GHRS/G140L‡	4	...
...	...	621	...	97	445	2981	O3–4 V+O4–7 V	Wa14	053838.026-690543.30	13.80	13.58	14.79	S	(0.25)	(O3.5 V)
...	...	69	O4–5 V	Be20	14.02	15.05	D,H	(0.25)	GHRS/G140L‡	4	...
...	...	65	O4 V	Cr16	14.03	15.18	D	(0.24)	(O4 V)
...	...	64	O4–5 V	Be20	053842.646-690601.05	13.83	13.95	14.53	S	(0.24)	(O4 V)
...	...	78	O4: V	Be20	14.04	15.26	D	(0.24)	GHRS/G140L‡	4	...
...	...	324	...	131	393	2256	O9.5(n)	Wa14	053832.992-690513.05	13.87	14.04	15.26	S	(0.24)	(O9.5 III)
...	...	977	...	139	...	2893	O6: V	Bo99	053842.636-690538.69	13.88	14.12	15.36	S	(0.23)	(O6 V)
...	...	1222	...	116	...	3180	O3–6 V	WB97	053845.150-690508.34	13.88	14.08	14.99	S	(0.23)	(O4.5 V)
...	...	73	O9.7–B0 V	Be20	14.12	15.13	D	(0.23)	GHRS/G140L‡	4	...
...	...	1594	...	125	661	2691	O6.5 V+O9.7 V	Wa14	053852.049-690533.79	13.94	14.00	15.19	S	(0.22)	(O6 V)
...	...	1295	...	137	596	1325	O7–8 V	Wa14	053846.059-690615.55	13.97	14.25	15.35	S	(0.21)	(O7 V)
...	...	884	...	143	511	1008	O5 Vz	Wa14	053841.717-690628.13	13.98	14.21	15.31	S	(0.21)	(O4.5 V)
...	...	95	155	...	1920	...	O4:	Ca21	053840.949-690555.14	14.00	14.26	15.43	S	(0.21)	(O4 III)
...	...	84	145	...	1956:	...	O5:	Ca21	14.20	14.80	H	(0.21)	(O5 III)
...	...	92	O6 Vz	Be20	14.20	15.46	D	(0.21)	GHRS/G140L‡	4	...
...	...	1026	68	127	...	1787	O4–5 V	Be20	053843.180-690601.73	14.01	14.10	14.80	S	(0.21)	(O4.5 V)
...	...	1141	109	169	1035	2129	O8.5 I-II	He12	053844.312-690545.10	14.01	14.29	15.57	S	(0.21)	(O8.5 I)
...	...	970	83	142	1023	1580	O8 III-V	He12	053842.618-690610.00	14.02	14.22	15.31	S	(0.20)	(O8 III)
...	...	90	O4: V:	Be20	14.24	15.48	D	(0.20)	GHRS/G140L‡	4	...
...	141	373	2090	...	O9.5n	Wa14	053831.224-690553.03	...	14.24	15.27	S	(0.20)	(O9.5 III)
...	...	1191	...	128	575	2804	B0.7 III	Ev15	053844.904-690533.13	13.76	13.99	15.12	S	(0.20)	(B1 III)
...	...	88	165	1009	1732	...	O6.5 V–III	He12	053841.147-690602.91	14.07	14.23	15.42	S	(0.20)	(O6.5 III)
...	...	108	O7–8 V	Cr16	14.27	15.44	D	(0.20)	(O7 V)
...	...	729	138	144	...	1535	O5:	Ca21	053839.700-690608.63	14.08	14.20	15.31	S	(0.19)	(O5 III)
...	...	96	163	1008	1852	...	ON6.5 II–I	He12	053841.093-690558.40	14.09	14.32	...	S	(0.19)	(O6 I)
...	...	957	99	167	...	1527	O8 V	MH98	053842.445-690609.22	14.11	14.32	15.41	S	(0.19)	(O8 V)
...	...	1527	...	119	646	1951	B0.5 III(n)	Ev15	053850.263-690604.37	13.84	14.03	14.99	S	(0.19)	(B0 III)
...	...	93	O4–5 V	Cr16 ^a	14.34	15.60	H	(0.18)	GHRS/G140L‡	4	...
...	...	531	...	166	...	1941	O8 V	Bo99	053836.728-690556.46	14.15	14.32	15.54	S	(0.18)	(O8 V)
...	...	740	...	159	...	1537	O6:	Ca21	053839.837-690607.99	14.15	14.29	15.41	S	(0.18)	(O6 III)
...	...	94	O4–5 Vz	Be20	14.36	15.57	D	(0.18)	GHRS/G140L‡	4	...
...	...	1031	...	152	543	2521	O9 IV+O9.7: V	Wa14	053843.190-690527.52	14.17	14.26	15.44	S	(0.18)	(O9 V)
...	...	1288	...	175	597	375	O8–9 V(n)	Wa14	053846.063-690656.16	...	14.38	15.62	S	(0.18)	(O9 V)
...	...	1468	...	174	635	1334	O9.5 IV	Wa14	053849.039-690619.57	...	14.39	15.56	S	(0.18)	(O9 V)
...	...	101	178	1020	1401	...	O3–4	He12	053842.012-690616.83	14.21	14.40	15.53	S	(0.17)	(O3.5 V)
...	...	1145	...	168	561	2301	O9:(n)	Wa14	053844.368-690514.36	...	14.41	15.46	S	(0.17)	(O9 III)
...	...	901	...	138	518	1068	O3.5 III(f*)	Wa14	053841.934-690629.70	14.21	14.24	15.15	S	(0.17)	(O3 III)
...	...	887	85	154	1016	1371	O8 V	Bo99	053841.755-690619.06	14.22	14.33	15.31	S	(0.17)	(O8 V)
...	...	1336	...	176	...	2945	O8:	Ca21	053846.481-690542.20	14.22	14.39	15.54	S	(0.17)	(O8 III)
...	...	114	O5–6 V	Be20	14.43	15.68	D	(0.17)	(O5.5 V)
...	...	198	3167	...	O8:	Ca21	053841.818-690507.18	14.23	14.48	15.76	S	(0.17)	(O8 III)

Table B1. (continued)

R	Mk	P	HSH	SMB	VFTS	CCE	SpT	Ref	HTTP	m_{275W}	m_{F336W}	m_{F555W}	Ref	F_{1500}	10^{-13}	Spectrum	Ref	VMS
										mag	mag	mag			(Template)			
...	...	841	98	157	...	2016	O4–6(n)(f)p	WB97	053841.186-690552.12	14.25	14.42	15.45	S	(0.17)	(O5 III)	
...	...	100	B0 V	MH98	053842.206-690614.82	14.27	14.52	15.64	S,H	(0.17)	(B0 V)	
...	992	...	182	...	2665	O7:	Ca21	053842.838-690530.36	14.29	14.44	15.56	S	(0.16)	(O7 III)		
...	485	...	158	419	2897	O9: V(n)	Wa14	053835.906-690534.95	14.32	14.33	15.41	S	(0.16)	(O9 V)		
...	...	113	190	...	1503	O9 V	MH98	053842.243-690612.23	14.32	14.53	15.62	S	(0.16)	(O9 V)		
...	796	...	185	...	2565	O6:	Ca21	053840.665-690531.16	14.32	14.42	15.59	S	(0.16)	(O6 III)		
...	670	...	172	456	2385	Onn(f)	Wa14	053838.818-690525.56	14.34	14.42	15.45	S	(0.15)	(O6 III)		
...	994	...	146	...	2270	B0: V	Bo99	053842.841-690514.80	14.07	14.19	15.44	S	(0.15)	(B0 V)		
...	1201	...	171	579	3116	O9:((n))	Wa14	053844.969-690507.65	14.36	14.56	15.47	S	(0.15)	(O9 V)		
...	...	141	O5–6 V	Cr16	14.56	15.82	D	(0.15)	GHRS/G140L‡	4	...		
...	...	116	O7 V	Be20	14.57	15.79	D	(0.15)	(O7 V)		
...	...	115	O9+ V	Cr16	14.57	15.76	D	(0.15)	(O9 V)		
...	1359	...	202	...	2782	O8:	Ca21	053846.901-690536.82	14.37	14.59	15.78	S	(0.15)	(O8 III)		
...	1560	...	200	654	3010	O9 Vnn	Wa14	053851.159-690541.81	14.38	14.62	15.77	S	(0.15)	(O9 V)		
...	...	179	570	3134	O9.5ne+	Wa14	053844.684-690545.19	14.39	14.42	...	S	(0.15)	(O9.5 III)			
...	578	...	209	436	2223	O7–8 V	Wa14	053837.348-690521.29	14.39	14.58	15.93	S	(0.15)	(O7 V)		
...	...	112	O7–9 Vz	Be20	14.61	15.74	D	(0.14)	GHRS/G140L‡	4	...		
...	...	224	660	3027	O9.5 Vnn	Wa14	053851.812-690546.85	14.43	14.76	16.00	S	(0.14)	(O9 V)			
...	132	O7: V	Be20	14.64	15.86	D	(0.14)	(O7 V)		
...	348	...	227	400	2607	O9.7	Be20	053833..536-690521.73	14.45	14.79	16.05	S	(0.14)	(O9.5 III)		
...	...	212	...	2776	O8:	Ca21	053843.127-690537.76	14.51	14.67	15.89	S	(0.13)	(O8 III)			
...	490	...	140	422	1373	O4 III(f)	Wa14	053835.993-690616.91	14.15	14.23	15.15	S	0.13	COS/G140L	2	...		
...	...	123	O6 V	Be20	053842.043-690604.58	14.52	14.71	15.76	S	(0.13)	(O6 V)		
...	...	121	O9.5 V	Be20	14.73	15.85	D	(0.13)	(O9 V)		
...	...	134	O7 Vz	Be20	053842.182-690604.95	14.52	14.74	15.44	S	(0.13)	(O7 V)		
...	206	476	2789	O((n))	Wa14	053839.734-690539.27	14.53	14.73	15.72	S	(0.13)	(O6 III)		
...	444	O9.7	Wa14	053838.011-690508.53	14.55	14.86	16.12	S	(0.13)	(B0 V)		
...	...	218	615	1398	O9.5 IIIInn	Wa14	053847.320-690617.74	...	14.78	15.64	S	(0.12)	(O9.5 III)			
...	881	...	215	...	2389	O9:	Ca21	053841.643-690523.77	14.58	14.69	15.87	S	(0.12)	(O9 III)		
...	...	118	O7–8 V	Cr16	14.79	15.89	D	(0.12)	(O8 V)		
...	...	211	...	1415	O7:	Ca21	053843.317-690611.65	14.61	14.80	15.92	S	(0.12)	(O7 III)			
...	743	...	151	...	1523	O6:	Ca21	053839.846-690609.50	14.61	14.83	15.40	S	(0.12)	(O6 III)		
...	918:	...	311:	...	1522	O7:	Ca21	053842.067-690608.95	...	14.82	15.81	S	(0.12)	(O7 III)		
...	...	194	446	1339	Onn	Wa14	053838.245-690617.36	14.62	14.63	15.46	S	(0.12)	(O9.5 V)			
...	915	144	238	...	2130	O8:	Ca21	053842.061-690552.23	14.62	14.85	15.97	S	(0.12)	(O8 III)		
...	...	103	189	1010	1346	O7 V–III	Ma12	053841.255-690617.02	14.65	14.69	15.55	S	(0.11)	(O7 III)		
...	...	226	382	2901	O4–5 V	Wa14	053832.253-690544.58	14.66	14.82	15.93	S	(0.11)	(O4.5 V)			
...	...	140	187	1015	1734	O8: V	Le21	053841.637-690603.25	14.66	14.83	15.76	S	(0.11)	(O8 V)		
...	...	208	443	1557	O7: V	Wa14	053837.972-690615.30	14.67	14.75	15.73	S	(0.11)	(O7 V)			
...	547	...	214	432	466	O8–9 V	Wa14	053837.030-690650.70	...	14.88	15.73	S	(0.11)	(O8 V)		
...	1369	...	219	613	2005	O8.5 Vz	Wa14	053847.161-690554.46	14.68	14.80	15.80	S	(0.11)	(O8 V)		
...	853	...	177	1011	1447	O5 V	Le21	053841.348-690614.04	14.70	14.75	15.39	S	(0.11)	(O4.5 V)		
...	...	126	193	1004	1725	O9.5 V–III	He12	053840.831-690604.60	14.70	14.82	15.59	S	(0.11)	(O9.5 III)		
...	803	...	213	491	276	O6 V	Wa14	053840.846-690657.51	...	14.96	15.69	S	(0.10)	(O6 V)		
...	...	239	649	2038	O9.5 V	Wa14	053850.610-690554.57	14.77	15.02	16.14	S	(0.10)	(O9 V)			
...	1224	...	231	...	1472	O6:	Ca21	053845.213-690613.62	14.78	14.90	15.99	S	(0.10)	(O6 III)		
...	...	277	...	2453	O8:	Ca21	053840.166-690520.63	14.78	15.04	16.34	S	(0.10)	(O8 III)			
...	1401	...	234	619	689	O7–8 V(n)	Wa14	053847.717-690644.94	...	14.99	16.07	S	(0.10)	(O8 V)		
...	...	102	207	O2–3 III	Cr16	053843.165-690600.85	14.79	14.79	15.52	S	(0.10)	(O2.5 III)		
...	1087	...	272	...	1275	O8:	Ca21	053843.749-690621.89	14.79	15.06	16.27	S	(0.10)	(O8 III)		
...	1086	...	247	...	2454	O7:	Ca21	053843.709-690521.64	14.80	14.97	16.16	S	(0.10)	(O7 III)		
...	982	160	258	...	2044	O4: V	Pa93	053842.721-690552.80	14.80	14.98	16.14	S	(0.10)	(O4 V)		

Sp Types: Be20: [Bestenlehner et al. \(2020\)](#); Be22: [Bestenlehner et al. \(2022\)](#); Bo99: [Bosch et al. \(1999\)](#); Ca21: [Castro et al. \(2021b\)](#); Cr10: [Crowther et al. \(2010\)](#); Cr16: [Crowther et al. \(2016\)](#); Cr22: [Crowther et al. \(2022\)](#); CD98: [Crowther & Dessart \(1998\)](#); CS97: [Crowther & Smith \(1997\)](#); CW11: [Crowther & Walborn \(2011\)](#); De97: [de Koter et al. \(1997\)](#); Do13: [Doran et al. \(2013\)](#); Ev11: [Evans et al. \(2011\)](#); Ev15: [Evans et al. \(2015\)](#); He12: [Hénault-Brunet et al. \(2012\)](#); Ka22: [Kalari et al. \(2022\)](#); Le21: D. Lennon (priv comm, 2021); Ma02: [Massey et al. \(2002\)](#); Ma05: [Massey et al. \(2005\)](#); Ma12: [Massey et al. \(2012\)](#); MH98: [Massey & Hunter \(1998\)](#); Pa93: [Parker \(1993\)](#); Te19: [Tehrani et al. \(2019\)](#); Wa14: [Walborn et al. \(2014\)](#); WB97: [Walborn & Blades \(1997\)](#).

Spectroscopy: 1. GO 16272 (Shenar); 2. GO 15629 (Mahy); 3. Roman-Duval et al. (2020); 4. [Heap et al. \(1992\)](#); 5. [de Koter et al. \(1998\)](#); 6. [Massey et al. \(2005\)](#). Note: (a) spectral type of HSH 119 (fainter component of blend with $m_{F336W} = 15.0$ mag)

Photometry: D: [De Marchi et al. \(2011\)](#); H: [Hunter et al. \(1995\)](#); S: [Sabbi et al. \(2016\)](#)

Table B2. Stars within the *IUE* 3×3 arcmin 2 Vacca et al. (1995) field of view which are exterior to MUSE, sorted by far-UV flux (F_{1500} units of erg s $^{-1}$ cm $^{-2}$ Å $^{-1}$), measured from *IUE/SWP* spectroscopy or estimated from photometry, the latter indicated in parentheses. See Table B1 for references in common.

R	Mk	P	HSH	SMB	VFTS	CCE	SpT	Ref	HTTP	m_{275W}	m_{F336W}	m_{F555W}	Ref	F_{1500}	Spectrum	Ref	VMS
										mag	mag	mag		10^{-13}	(Template)		
139	...	952	...	2	527	...	O6.5 Iafc+O7 Iaf	Wa14	053842.351-690458.19	10.97	10.86	12.02	S	6.21	(O7 I)	1	...
145	...	1788	695	...	WN6h+O3/5 If/WN7	Sh17	053857.072-690605.58	...	10.88	11.94	S	4.21	(WN6)	1	✓
135	...	355	...	12	402	...	WN5:+WN7	Sh19	053833.615-690450.47	11.63	11.68	12.82	S	2.34	(WN6)	1	...
...	23	1163	...	42	566	...	O3 III(f*)	Wa14	053844.558-690451.19	12.40	12.68	14.03	S	(0.91)	(O3 III)
...	...	1035	O3–6 V	WB97	053843.159-690441.82	12.93	13.35	14.75	S	(0.56)	(O4.5 V)
...	57	541	...	79	429	...	O7:V+B1:V	Sh22	053836.854-690458.28	12.95	13.32	14.70	S	(0.55)	(O7 V)
...	...	809	...	133	O8–9 V	Bo99	053840.773-690452.83	13.67	14.01	15.34	S	(0.28)	(O9 V)
...	...	1077	550	...	O5 V((f))z	Wa14	053843.599-690442.44	13.78	14.12	15.42	S	(0.26)	(O5 V)
...	...	124	350	...	O8.5 V+O9.5 V	Sh22	053828.057-690629.05	13.79	14.09	15.03	S	(0.25)	(O9 V)
...	...	83	339	...	O9.5 IV	Wa14	053826.218-690501.84	13.83	14.15	15.52	S	(0.24)	(O9 V)
...	...	169	...	107	360	...	O9.7	Wa14	053829.421-690521.20	13.84	13.85	14.85	S	(0.24)	(O9.5 III)
...	...	466	...	150	415	...	O9.5 V	Wa14	053835.480-690457.67	13.90	14.17	15.50	S	(0.23)	(O9 V)
...	60	195	...	98	363	...	B0.2 III-II	Ev15	053829.986-690505.18	13.61	13.68	14.86	S	(0.23)	(B0 III)
...	...	1052	546	...	O8–9 III	Wa14	053843.373-690446.34	14.02	14.21	15.41	S	(0.20)	(O8 III)
...	...	1729	686	...	B0.7 III	Ev15	053855.634-690723.71	14.05	14.15	15.05	S	(0.15)	(B1 III)
...	...	1756	688	...	O9.7 III	Wa14	053856.058-690554.04	14.45	14.70	15.64	S	(0.14)	(O9.5 III)
...	...	955	529	...	O9.5(n)	Wa14	053842.374-690443.12	14.55	14.89	16.09	S	(0.13)	(O9.5 III)
...	...	905	521	...	O9 V(n)	Wa14	053841.955-690704.97	...	14.82	15.90	S	(0.12)	(O9 V)
...	...	171	...	216	361	...	O8.5 V	Wa14	053829.482-690620.55	14.63	14.81	15.75	S	(0.12)	(O8 V)
...	...	1840	707	...	B0.5 V	Ev15	053858.907-690642.05	...	14.55	15.65	S	(0.12)	(B0.5 V)
...	486	...	B1-2ne+	Ev15	053840.604-690456.02	14.20	14.16	15.28	S	(0.11)	(B1 III)
...	319	412	...	O9.7	Wa14	053834.901-690453.74	14.71	15.14	16.47	S	(0.11)	(O9.5 III)
...	...	1209	...	205	O9–B0 V	Bo99	053845.055-690446.88	14.74	14.85	15.67	S	(0.11)	(O9 V)
...	...	1429	621	...	O2 V((f))z	Wa14	053848.089-690442.18	14.80	14.86	15.59	S	(0.10)	(O2 V)

Sp Types: Sh17: Shenar et al. (2017); Sh19: Shenar et al. (2019); Sh22: Shenar et al. (2022)

Spectroscopy: 1. Fitzpatrick & Savage (1984)

APPENDIX C: FAR-UV CALIBRATIONS

We calibrate F_{1500} fluxes against m_{F275W} or F_{F336W} photometry using reference O stars in 30 Doradus that have been observed in the far-UV. These are listed in Table C1, sorted by F_{1500} with references to spectral types, photometry and HST datasets identical to Table B1. Column densities, $\log N(\text{H}\alpha)$ from fits to Ly α are included and should be reliable to ± 0.05 dex (e.g. Welty et al. (2012) obtain $\log N(\text{H}\alpha/\text{cm}^2) = 21.79$ for Mk 42). Comparisons are presented in Fig. 3, with calibrations presented in Eqn 1-2. Since we utilise templates spanning a range of extinctions, we also adjust far-UV slopes ($\lambda\lambda 1160-1700$) of templates to individual O stars within the MUSE field from their $m_{F336W} - m_{F555W}$ colours. These are presented in Fig. C1 with the fit obtained as follows

$$F_{1700}/F_{1160} \approx 1.76(m_{F336W} - m_{F555W}) + 3.33. \quad (\text{C1})$$

30 Doradus O stars external to the MUSE field reveal a somewhat different behaviour, likely as a result of lower dust extinction.

This paper has been typeset from a $\text{\TeX}/\text{\LaTeX}$ file prepared by the author.

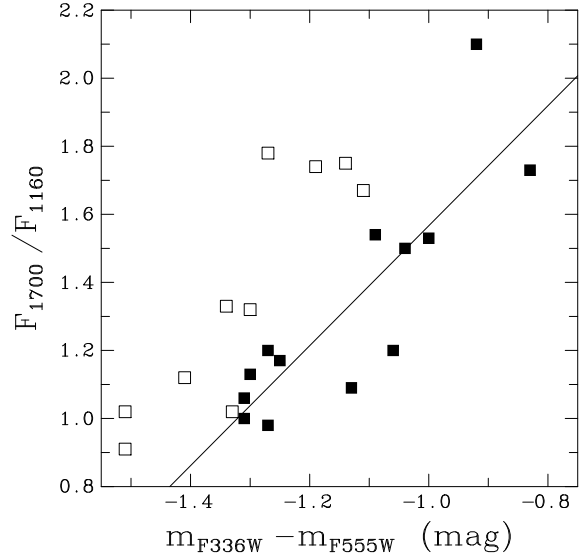


Figure C1. Relationship between $(m_{F336W} - m_{F555W})$ colour and far-UV slope, F_{1700}/F_{1160} , for O stars in 30 Doradus (solid within MUSE field) with far-UV spectroscopy and HST/WFC3 photometry. The solid line is a linear fit to observations within the MUSE field.

Table C1. Reference O stars within 30 Doradus used to calibrate far-UV fluxes (units are $\text{erg s}^{-1} \text{cm}^{-2} \text{\AA}^{-1}$), $\lambda\lambda 1160\text{-}1700$ slopes and $\log N(\text{H}\alpha)$ from fits to Ly α . Sources within MUSE footprint are indicated. References are as for Table B1.

Star	Sp Type	Ref	m_{F275W} (mag)	m_{F336W} (mag)	m_{F555W} (mag)	Ref	F_{1500} 10^{-13}	F_{1700}/F_{1160}	$\log N(\text{H}\alpha)$ cm^{-2}	HST dataset	Ref	MUSE
Mk 42	O2 If	CW11	11.08	11.51	12.82	S	3.01	1.00	21.75	STIS/E140M	3	✓
Mk 39	O2.5 If/WN6+	Cr22	11.38	11.66	12.95	S	2.74	1.13	21.75	COS/G130M+G160M	3	✓
VFTS 506	ON2 V	Wa14	11.74	12.01	13.32	S	2.04	1.06	21.8	COS/G130M+G160M	3	✓
Mk 30	O2 If/WN5	CW11	11.91	12.22	13.48	S	1.85	0.98	21.75	COS/G130M+G160M	3	✓
VFTS 180	O3 If*	Wa14	...	12.11	13.52	S	1.57	1.12	21.6	COS/G130M+G160M	3	...
VFTS 87	O9.7 Ib-II	Wa14	11.97	12.09	13.60	S	1.52	1.02	21.6	STIS/E140M	3	...
VFTS 267	O3 III-I	Wa14	...	12.15	13.49	S	1.39	1.33	21.75	COS/G130M+G160M	3	...
VFTS 440	O6–6.5 III	Wa14	12.15	12.44	13.69	S	0.96	1.17	21.75	STIS/E140M	2	✓
Mk 37a	O3.5 If/WN7	CW11	12.33	12.48	13.52	S	0.82	1.50	...	STIS/G140L	6	✓
Mk 33S	O3 III	Ma15	12.48	12.76	13.81	S	0.79	1.20	...	STIS/G140L	6	✓
VFTS 586	O4 Vz	Wa14	13.06	13.50	15.02	S	0.76	0.91	21.75	COS/G130M+G160M	3	...
VFTS 352	O4.5 Vz+O5.5 Vz	Wa14	12.75	13.13	14.46	S	0.70	1.02	21.8	COS/G130M+G160M	3	...
Mk 55	O6 Vnn	Wa14	12.79	13.04	14.34	S	0.61	1.32	21.75	COS/G130M+G160M	3	...
VFTS 385	O4–5 V	Wa14	13.22	13.38	14.65	S	0.51	1.20	21.8:	COS/G140L	2	✓
VFTS 404	O3.5 V	Wa14	12.76	12.95	14.13	S	0.49	1.74	21.9	COS/G130M+G160M	3	...
Mk 51	O3.5 If/WN7	CW11	...	12.98	13.81	S	0.45	1.73	21.9:	COS/G140L	2	✓
Mk14S	O4 III	Wa14	13.01	13.19	14.29	S	0.43	1.54	21.9:	COS/G140L	2	✓
Mk 4	O7 II	Wa14	...	13.37	14.38	S	0.41	1.53	22.0:	COS/G140L	2	✓
VFTS 667	O6 V	Wa14	...	13.95	15.08	S	0.33	1.09	21.9:	COS/G140L	2	✓
VFTS 169	O2.5 V	Wa14	13.64	13.46	14.60	S	0.32	1.75	22.0	COS/G130M+G160M	3	...
VFTS 190	O7 Vnnp	Wa14	13.70	13.43	14.70	S	0.28	1.78	21.7	COS/G130M+G160M	3	...
VFTS 66	O9.5 III	Wa14	14.40	14.49	15.61	S	0.14	1.67	22.0	COS/G130M+G160M	3	...
VFTS 422	O4III(f)	Wa14	14.15	14.23	15.15	S	0.13	2.10	21.9:	COS/G140L	2	✓